

Understanding Injection Into High Pressure Supercritical Environments

*B. Chehroudi and D. Talley

Air Force Research Laboratory (AFRL), Propulsion Directorate

*Engineering Research Consultants

W. Mayer, R. Branam, J.J. Smith, A. Schik, and M. Oschwald

DLR Lampoldshausen, Institute of Space Propulsion, D-74239 Hardthausen, Germany

Abstract

This paper summarizes the results of systematic research programs at both the DLR and the AFRL which began nearly ten years ago. The research is aimed at improving the understanding of atomization, mixing, and combustion processes associated with coaxially injected liquid propellant rocket engines. Cold flow studies are imperative for investigations without the complexities introduced with combustion. Initial studies utilized liquid nitrogen (LN₂) without a co-flow stream into a chamber with ambient pressures exceeding the thermodynamic critical pressure of the injectant. Secondly, cryogenic cold flow studies were extended with consideration of the effects of a co-flowing gas. Parallel to this work, combustion studies with cryogenic propellants were introduced to understand high-pressure coaxial injection phenomena with the influence of chemical reaction. In both cases, high-pressure injection and combustion facilities were specifically designed and implemented to gain maximum information from a single coaxial injector element.

Results from visualization, jet initial growth rate, fractal analysis, Raman scattering, visible length scales, and phenomenological modeling are presented and discussed. It is found that the behavior of the injected jet into supercritical ambient is quite different from those at subcritical conditions. In particular, it is found that the nature of atomization is substantially different and departs significantly from the classical cascade of events attributed to low-pressure liquid jet atomization. At elevated pressure conditions, the injected cryogenic liquid jet behaves more like a high-density gas injected into a low-density gas environment. Implications of this behavior on mixing, growth rate, evolution and response of reacting and non-reacting flow-fields, combustion zone time and length scales, and combustor behavior are investigated and discussed.

Important data has been obtained for analysis and interpretation through the application of a range of non-intrusive optical diagnostics. Detailed descriptions of diagnostic techniques implemented are not provided herein due to size constraints. Furthermore, significant contributions to the field of high-pressure injection and combustion are referenced throughout the text where appropriate.

1 Introduction

1.1 Objectives of this paper

The main purpose of this joint paper by the DLR and the AFRL is to consolidate and compare findings related to the injection of cryogenic liquids into supercritical thermodynamic conditions. The hope is that by doing so, areas that require more concentration can be identified. The paper contains four major sections. The first section provides a description outlining the motivation behind the research undertaken by the groups, with a brief introduction to supercritical thermodynamic phenomena.

The second section focuses on high pressure single jet and coaxial jet cold flow, non-reacting studies, and a vast range of information resulting from this research. A brief description of the experimental setup is followed by details of the diagnostic and analysis techniques. A series of results are then presented and discussed in the following order: shadowgraphy and qualitative understanding, then quantitative analysis of the shadowgraphs including jet growth rate, fractal analysis, and length scale analysis. Further discussion is based on more quantitative approaches including Raman scattering diagnostics to map the density and temperature fields, visual length scale measurements, and acoustic / jet interactions. Finally, phenomenological modeling of the jet growth rate is presented.

Section Three provides a comprehensive overview of cryogenic propellant combustion studies at high pressure conditions, highlighting the important successes to date. Shadowgraphy of a reacting flow field is followed by a discussion of OH emission, indicating the reaction zones at supercritical conditions. A brief commentary on temperature measurements using laser diagnostics is provided, followed by investigations of combustion chamber response during operation. Section Four concludes the paper and highlights the advances made by the two groups in the field of high pressure injection and combustion studies.

1.2 Why do research under supercritical conditions?

By a simple thermodynamic analysis of the rocket engine thrust chamber, one can show that higher chamber pressures lead to a higher specific impulse for the engine. This has motivated a trend towards increasingly higher chamber pressure operation. A similar observation is also true for gas turbine and diesel engines to increase power output and efficiency. However, at higher pressures, the injected liquid may find itself near or above the thermodynamic critical pressure. The fluid is then injected at a supercritical pressure, but typically initially at a subcritical temperature. It then typically heats up beyond its critical temperature as it mixes and burns in the combustion chamber, a process which has sometimes been called “transcritical.” No reliable information about injection behavior existed prior to investigations by the groups. Typical liquid rocket engines operate at conditions above the thermodynamic critical point of the injected propellants. For example, the liquid hydrogen/liquid oxygen (LH₂/LOX) Vulcain engine chamber pressure in the Ariane 5 can reach up to a value of 11.5 MPa, while the combustion chamber pressure for the Space Shuttle Main Engine can reach as high as 22.3 MPa. The critical pressures and temperatures for relevant fluids and reactive propellants are listed in Table 1. The main objective of the investigations was to provide a better understanding of the atomization phenomena, mixing, flow instabilities, and flame stabilization under supercritical and transcritical conditions, leading to enhanced physical models for improved design methodologies.

Table 1: Critical Properties of Relevant fluids.

Critical Properties	N₂	He	O₂	H₂
Critical Pressure P_{crit} (MPa)	3.4	0.23	5.04	1.28
Critical Temperature T_{crit} (K)	126.2	5.2	154.6	32.94

1.3 Physical properties and issues specific to supercritical conditions

Surface tension plays a dominant role in the atomization process of liquid sprays, see Lefebvre [1]. A remarkable change in the atomization mechanisms from wind-induced capillary instability under sub-critical conditions to turbulent mixing with expansion under supercritical conditions has been observed. Within the supercritical atomization regime, liquid-gas-like break-up and gas-gas-like mixing behavior can be observed, see Pitts [2]. This process has been clearly observed from injection tests using non-reacting simulant cryogenic fluids such as LN₂ and He or H₂. Such cold flow experiments are discussed in the following section.

For coaxial injection of O₂ and H₂ (or simulant fluids) both components coalesce at the injectant interfaces and are mixed within the shear layer. Therefore one must use caution when discussing the thermodynamic state of the media. The critical point is no longer defined in a mixed binary system. Critical mixing lines define the thermodynamic state under such conditions experienced at the shear layer interface. The coaxial stream is typically gaseous and dissolves in the liquid phase, which causes a shift in the critical temperature in comparison to the pure liquid.

The phase diagram for the binary H₂/O₂-system is shown in Fig.1. For a given reduced pressure ($P_r = P_{\text{ch}}/P_{\text{critO}_2}$) there is a critical mixing temperature above which the mixture is in a supercritical state. Below the critical mixing temperature the binary system separates into a liquid and a gaseous phase. The concentration of the H₂/O₂ species is displayed in Figure 1 as two phases at a given temperature by the dashed and solid lines for the gaseous and liquid component respectively. As can be seen in Fig. 1, the solubility of H₂ in liquid O₂ increases with increasing temperature and the amount of hydrogen in the gaseous phase decreases. At the critical mixing temperature the species fractions in the gaseous and liquid phase are identical, the phase boundary disappears and supercritical conditions exist.

Figure 2 shows the critical mixing temperature as a function of pressure for the various binary systems of interest. Below the critical mixing temperature phase equilibrium with liquid and gas exists. Above this temperature the mixture exhibits supercritical behavior. The general trend is that the critical mixing temperature decreases with increasing pressure.

The surface tension of the binary H₂/O₂-mixture has been computed using the Macleod-Sugdon correlation (see Tully et al. [6] and Macleod [7]) and is shown in Fig. 3. The results indicate that at pressures above the critical pressure of the pure O₂-system, surface tension may be present in the binary H₂/O₂-system, as long as the temperature remains below the critical mixing temperature. This is of course consistent with the fact that the phase diagram in Figure 1 predicts two phases for these conditions.

Atomization of the liquid is commonly accompanied by a mixing process of species of different temperatures. At pressures near the critical point, density is a very sensitive function of temperature, see Fig. 4. At 4 MPa around 129 K, nitrogen varies its density up to 21% per degrees Kelvin. This reflects that transport of internal energy driven by the temperature gradients shows features specific for critical conditions. Approaching the critical point, the specific heat is

increasing and exhibits a singularity at the critical point. At pressures above the critical pressure, the specific heat is finite again but still shows a pronounced maximum at a temperature T^* , see Fig. 4. Figure 5 shows the thermal diffusivity of the nitrogen as a function of temperature and pressure. As is shown in Fig. 5, the points (P, T^*) form a line continuing the coexistence line to higher pressures. The maximum of the specific heat at T^* is reflected in the behavior of the thermal diffusivity, see Fig. 5.

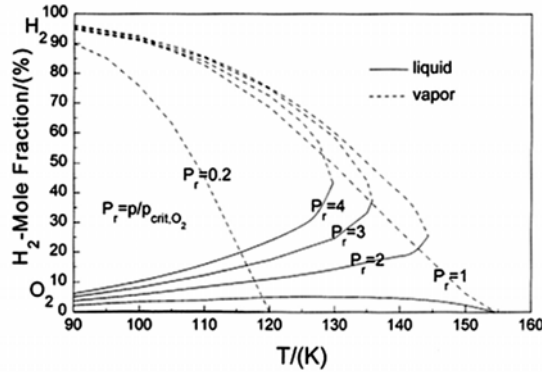


Figure 1: Phase equilibrium of the binary O_2/H_2 system

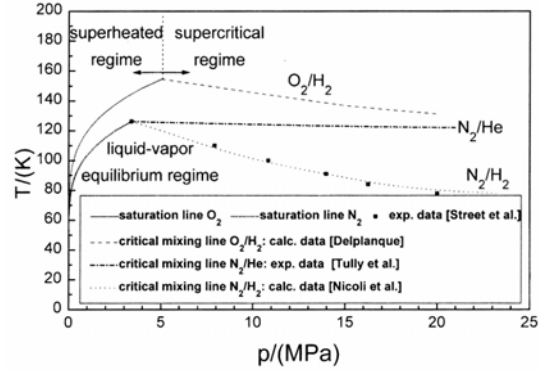


Figure 2: Critical mixing lines for binary O_2/H_2 , N_2/He , and N_2/H_2 -systems (Refs.[3], [4], [5], [6])

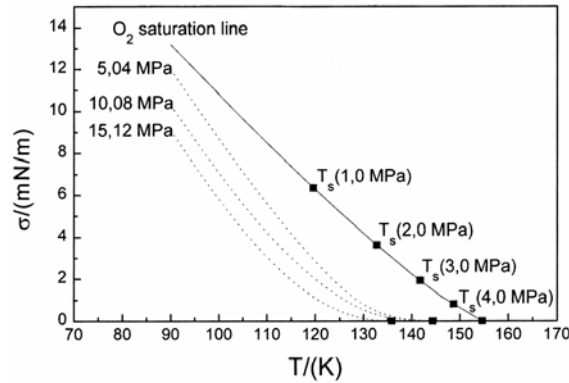


Figure 3: Phase equilibrium of the O_2/H_2 binary system

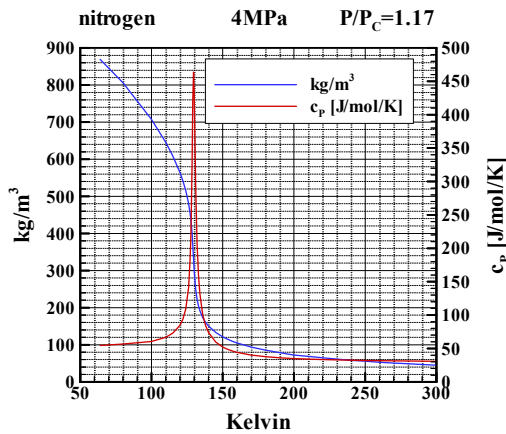


Figure 4: Density and specific heat of N_2 in the region near the critical point. $T^* = 129.5K$

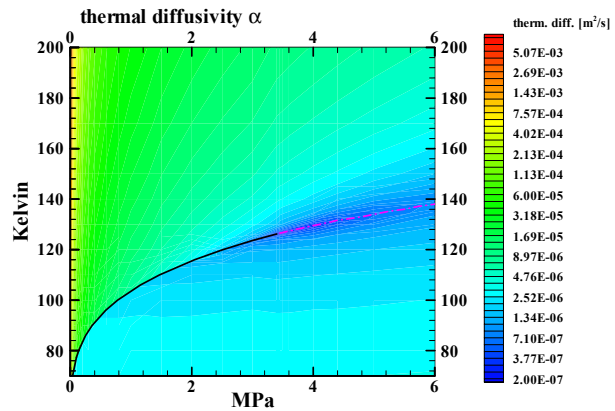


Figure 5: Thermal diffusivity of N_2 in the region near the critical point. Dashed line: T^* as a function of P .

2 Cold Flow Studies

2.1 Single jet

In a quest to understand liquid breakup mechanisms for injection under supercritical and transcritical conditions, researchers at DLR and AFRL began working with the simplest and perhaps the most popular and fundamental of all cases; i.e., injection of a single round jet under high pressures. Chamber pressures investigated were representative of those experienced in typical cryogenic liquid rocket engines, whereby a fluid is injected into a chamber at conditions exceeding the thermodynamic critical pressure (i.e., supercritical). The need for a high pressure chamber with sufficient optical access was obvious, and both research laboratories based their respective designs on this fact. Detailed information on these facilities has already been published in the past, and only key features are highlighted here.

Diagnostics tools applied in the past include high-speed shadowgraphy and Raman laser scattering at both the DLR and AFRL. Currently, preparations for the use of Laser Induced Thermal Acoustics (LITA) for pointwise temperature measurements are being made at AFRL, and results will be published in the near future. The cold flow results acquired by the groups were interpreted and analyzed both qualitatively and quantitatively. The purpose of this section of the paper is to present key findings by the groups and to highlight independently confirmed conclusions regarding single-jet injection under supercritical, non-reacting conditions. Areas that require further attention are also identified.

The term *supercritical* is used in reference to the chamber pressure and temperature being above the thermodynamic critical point of the injectant. The focus of most of the cold-flow experiments was on the injection of liquid nitrogen (LN_2) into a gaseous nitrogen (GN_2) environment. This eliminated confusion regarding any uncertainties existing in relation to the true supercritical state for mixtures. With a single working medium, well-defined thermodynamic properties and parameters, such as the location of the critical point, simplified data analysis and interpretation. Despite this, injection into other ambient gases was also investigated.

2.1.1 Description of experimental setup

Both laboratories have utilized a specially-designed, high pressure facility for these studies. The test-rig designs are somewhat different. However, both groups share a common goal. Basically, the AFRL facility is much smaller in physical scale. Details of each facility can be found in previous publications by the groups, many of which are listed in the extensive references section of this paper. However, adequate information regarding the injector geometries and Raman optical setup are necessary to better understand the results presented here.

Results from two different injectors were reported by the DLR, one with a diameter of 1.9 mm and L/D of 11.6 in early studies, and more recently, with a 2.2 mm diameter and L/D of 40. Depending on the Reynolds number, an entrance length of 40 to 100 is needed in order to have a fully-developed profile at the exit of the injector. The AFRL group reported results from an injector with a diameter of 0.254 mm and L/D of 200 for shadowgraphy and a 0.508 mm diameter tube with an L/D of 100 for Raman studies.

Two different optical setups were used by the DLR for Raman measurements. Oschwald and Schik [8] used spontaneous Raman scattering employing a cw ArIon laser operating at 488nm, whereas Branam and Mayer [9] reported resonant Raman using a XeF excimer laser at 351 nm

with two independent laser tubes operating in a double oscillator configuration. The two laser tubes fired with a short delay to reduce the peak intensity of the laser and to increase the total pulse length to about 40 ns in order to avoid gas optical breakdown. At AFRL, Chehroudi et al. [10] used a frequency-doubled Nd:Yag pulsed laser (532 nm output wavelength) with a passive pulse stretcher designed to reduce the possibility of plasma formation. The original pulse was extended in time by dividing it into three major pulses, each being 10 ns in duration, but delayed in time by 8 ns and 16 ns. This resulted in a final pulse duration of about 26 ns. The scattered Raman signal was collected at 607 nm.

2.1.2 Shadowgraphy and Visual Observation

Short-duration shadowgraphy is one effective method to gather information on the jet structure and document the effects of design and operating parameters on the flow field. Figure 6 (top row) shows representative images of a jet of LN₂ ($P_{cr} = 3.39$ MPa, $T_{cr} = 126.2$ K) injected at an initial temperature of 99-110 K into ambient temperature (300 K) gaseous nitrogen (GN₂). For the results presented here, the chamber pressure is normalized (or reduced) by the critical pressure of the injected media; P_r (i.e., reduced pressure) = $P_{chamber}/P_{cr}$. Considering the cryogenic nature of the injectant, it is important to establish whether the evolution of the jet within the region of interest is affected by buoyancy forces. Therefore, Froude number values were calculated at each condition. As an example, Chehroudi et al. [11 and 12] showed that for their experiments this number ranges from 42,000 to 110,000. Chen and Rodi [13] suggested that the flow is momentum dominated when a defined constant $x_b < 0.53$, while Papanicolaou and List [14] suggested $x_b < 1$. The length scale is given by $x_b = Fr^{-1/2}(\rho/\rho_\infty)^{-1/4}(x/d)$, where x is the axial distance, d is the initial jet diameter, ρ and ρ_∞ are the jet and ambient densities, respectively. The Froude number is defined as $Fr \equiv \rho U^2 / g d |\rho_\infty - \rho|$ where U is the velocity difference, g is the gravitational acceleration, and x_b is a constant. Considering the more conservative estimate by Chen and Rodi [13], the jet used by them is momentum dominated for distances less than 30 to 40 mm from the injector exit. Pictures presented in Fig. 6 cover up to about 5.5 mm (axial distance/diameter ratio of 21.6) from the injector, and hence buoyancy effects can be ignored in favor of the inertial forces.

The bottom row of Fig. 6 shows the jet shear layer. Generally, it is apparent that as pressure is increased, the jet width increases and the shear layer structures change from large-scale surface ligaments and droplets to more finger-like dominated structures. The results presented here are not unique to the injection of liquid nitrogen. Similar results have been found injecting liquid oxygen into gaseous nitrogen. In column (a), where the chamber pressure is subcritical, the jet has a classical liquid-like appearance. Consistent with the classical liquid jet breakup regimes described by Reitz and Bracco [15], surface instabilities grow downstream from the injector, and very fine ligaments and drops are ejected from the jet. This has been confirmed to correspond to the second wind-induced liquid jet breakup regime in Reitz and Bracco [15].

Major structural and interfacial changes occur at $P_r = 1.03$. Above this P_r , drops are no longer detected, and regular finger-like entities are observed at the interface. Rather than breaking up into droplets, the interface dissolves at different distances from the dense core. These structures are illustrated at a $P_r = 1.22$ in column (b) of Fig. 6. This change in the morphology of the mixing layer is evidently due to the combined effects of reductions in the surface tension as the critical pressure is exceeded and enthalpy of vaporization because of this transition.

As chamber pressure is further increased, the length and thickness of the dense core decreases, and the jet begins to appear similar to a turbulent gaseous jet injected into a gaseous environment. This is illustrated in Fig. 6, column (c). Any further droplet production, and consequently any additional classical liquid atomization, is completely suppressed. These observations were confirmed both at AFRL and DLR; for example, see Mayer et al. [16 and 17].

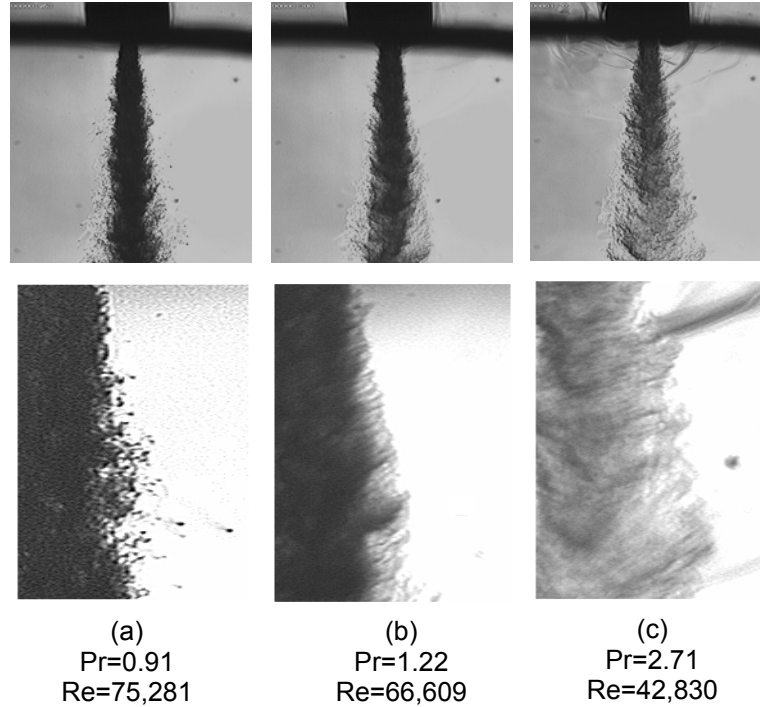


Figure 6: LN₂ injected into ambient temperature nitrogen at different pressures. The bottom row contains magnified images of the top row in order to examine the shear layer.

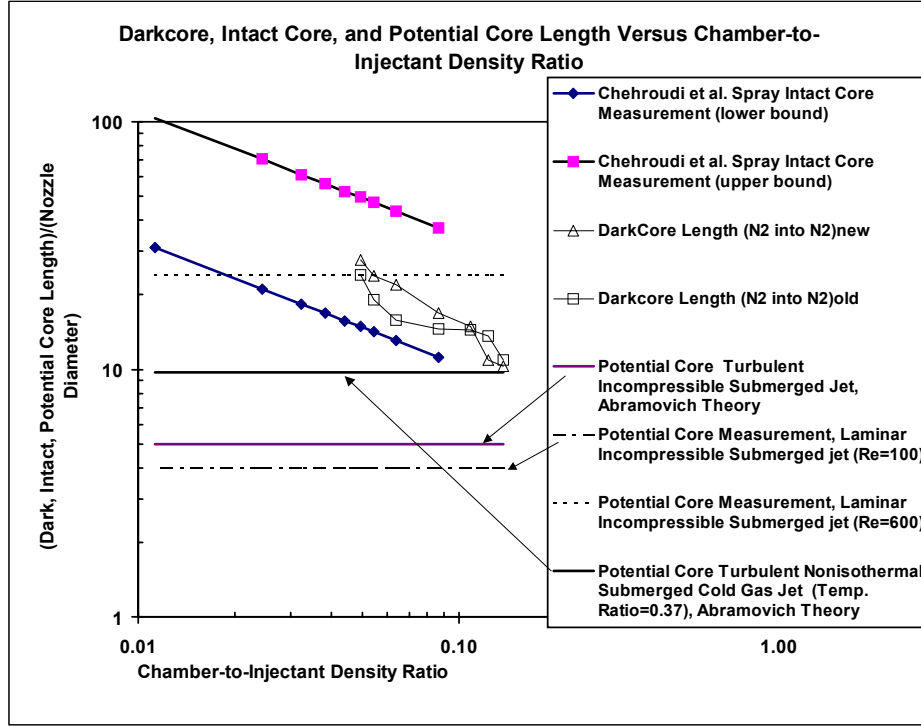
2.1.3 The dense core of the jet

According to Abramovich [18], the length of the potential core in isothermal uniform-density axisymmetric and two-dimensional jets is estimated to be about 6 to 10 injector diameters; whereas for non-isothermal cold jets injected into hot environments, it can reach up to about 25 injector diameters depending on jet temperature.

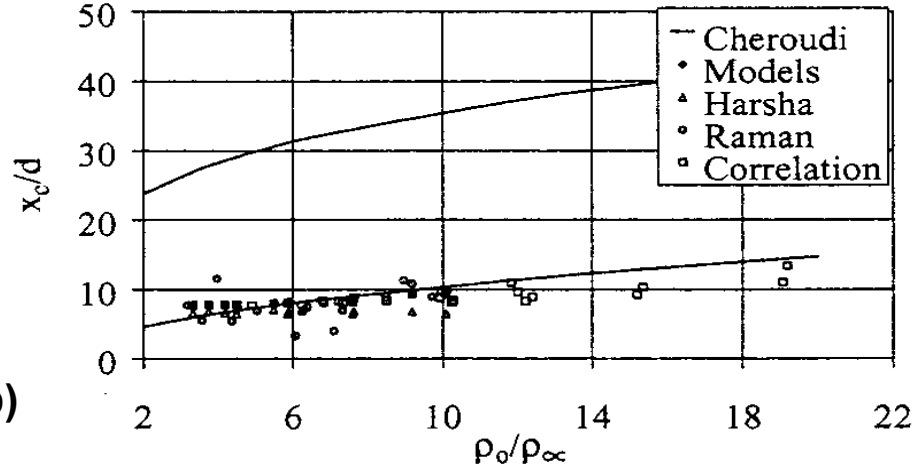
Also, according to Chehroudi et al. [19] the intact core length of the liquid sprays similar to the ones used in diesel engines is given by $Cd(\rho_l/\rho_g)^{1/2}$ where ρ_l and ρ_g are liquid injectant and chamber gas densities respectively, “d” is an effective jet exit diameter and C is a constant between 3.3 to 11. This translates to an intact core length between 33 to 110 injector diameters for the chamber-to-injectant density ratio of 0.01 and between 16.5 to 55 diameters for the chamber-to-injectant density ratio of 0.04. These results are presented in Fig. 7 (a) and (b) for better comparison.

Note that the classical two-stream mixing layer starts from the injector exit to approximately the end of the potential core (or intact core) of the jet. Assuming that the jet dark-core seen in images plays the same role as the intact core or potential core, Fig. 7 (a) indicates that growth rate data

(presented next) taken by Chehroudi et al. [12] is from the corresponding and appropriate initial region to ensure existence of a classical mixing layer. It is only then that a valid comparison can be made between these results and the two-stream mixing layers available in the literature.



(a)



(b)

Figure 7. (Dark-, intact- and potential- core length)/(nozzle diameter) as a function of chamber-to-injectant density ratio (case “a”) or injectant-to-chamber ratio (case “b”). Case a: Chehroudi et al. [12], determined by analysis of shadowgraphs, injector $L/D=200$. Case b: Branam and Mayer [9], determined via Raman data, injector $L/D=40$. Models: determined by computer simulation. Correlation: a correlation using set of Raman data by Branam and Mayer.

A complementary result by the DLR is shown in Fig. 7 (b). These results were determined through a log-log plot of the centerline intensity measured by Raman scattering to distinguish different flow regions. Note that the horizontal axis for Fig. 7 (a) and (b) are the inverse of each other. The DLR data are at or below the lower bound of the Chehroudi et al. [20] model (i.e., solid curve in Fig 7(b)) which was proposed based on the liquid sprays data in various atomization regimes. For chamber-to-injectant density ratios of less than 0.1 it appears that Chehroudi et al. data is larger by about a factor of 1.5 to 2 using the “correlation” data of Branam and Mayer [9] in Fig 7(b). Considering that the raw data used by the two groups are from two different methodologies, such a result is not unexpected. In fact, Chehroudi et al. [10] have also shown such differences when Raman and shadowgraphs were used in the context of growth rate measurements. However, improved techniques with more precise measurements are necessary in order to accurately assess this quantity.

2.1.4 The growth rate of the jet

Measurements and estimations of the growth rate of a jet has been a subject of intense research, because it provides a measure of mixing and development of the jet. Chehroudi et al. [11] were the first to extract quantitative measurements of this physical parameter from the images taken of a cryogenic LN₂ jet injected into GN₂ under both subcritical and supercritical environments. These measurements led to important results on the character of the growth rate and the behavior of the jet under such conditions.

The spreading angle or growth rate is measured from a field of view within 5.5 mm from the injector exit plane (distance-to-diameter ratio of up to 21.6). Results presented in Fig. 8 (a) indicate that the growth rate data collected by Chehroudi et al. [12] are from the corresponding and appropriate initial region to ensuring existence of a classical mixing layer. The initial jet spreading angle or its growth rate is measured for all acquired images, and results along with those of others are presented in Fig. 8. Of importance in this figure is the justification for the selection of the data sets and the nature of their measurements by other researchers. They are elaborated in sufficient details in earlier papers, and in order to possess a deeper appreciation of Fig. 8 and its uniqueness, see Chehroudi et al. [12]. Therefore, they are only mentioned here in brief as needed.

Since the jets investigated here exhibit both liquid-like and gas-like appearances, appropriate results for both are presented. The simplest is the prediction of the linear growth or constant spreading angle for the turbulent incompressible submerged jet using the mixing length concept. Following Abramovich [18] is a semi-empirical equation that attempts to incorporate the effects of density variations by the introduction of a characteristic velocity (see Chehroudi et al. [12]).

Brown and Roshko [21] measure spreading angles for a subsonic, two-dimensional, incompressible, turbulent mixing layer in which helium and nitrogen are used. Brown [22] (for temporally growing mixing layer) and Papamoschou and Roshko [23] proposed a theoretical equation for the incompressible variable-density mixing layer as shown in Fig. 8 (10 and 11 as well). Finally, Dimotakis [24] uses the observation that, in general, the entrainment into the mixing layer from each stream is not the same and, in a system moving with a convection velocity, offers a geometrical argument to derive an equation for the two-dimensional incompressible variable-density mixing layer (see Fig. 10).

Conversion of the two-dimensional mixing layer data for comparison with our initial growth rate is justified since, according to both Brown and Roshko, [21] and Abramovich et al. [18], two-

dimensional mixing layers are found to be fairly well approximated by the initial mixing region of axisymmetric jets. For this reason all angle measurements in Chehroudi et al. [12] works are

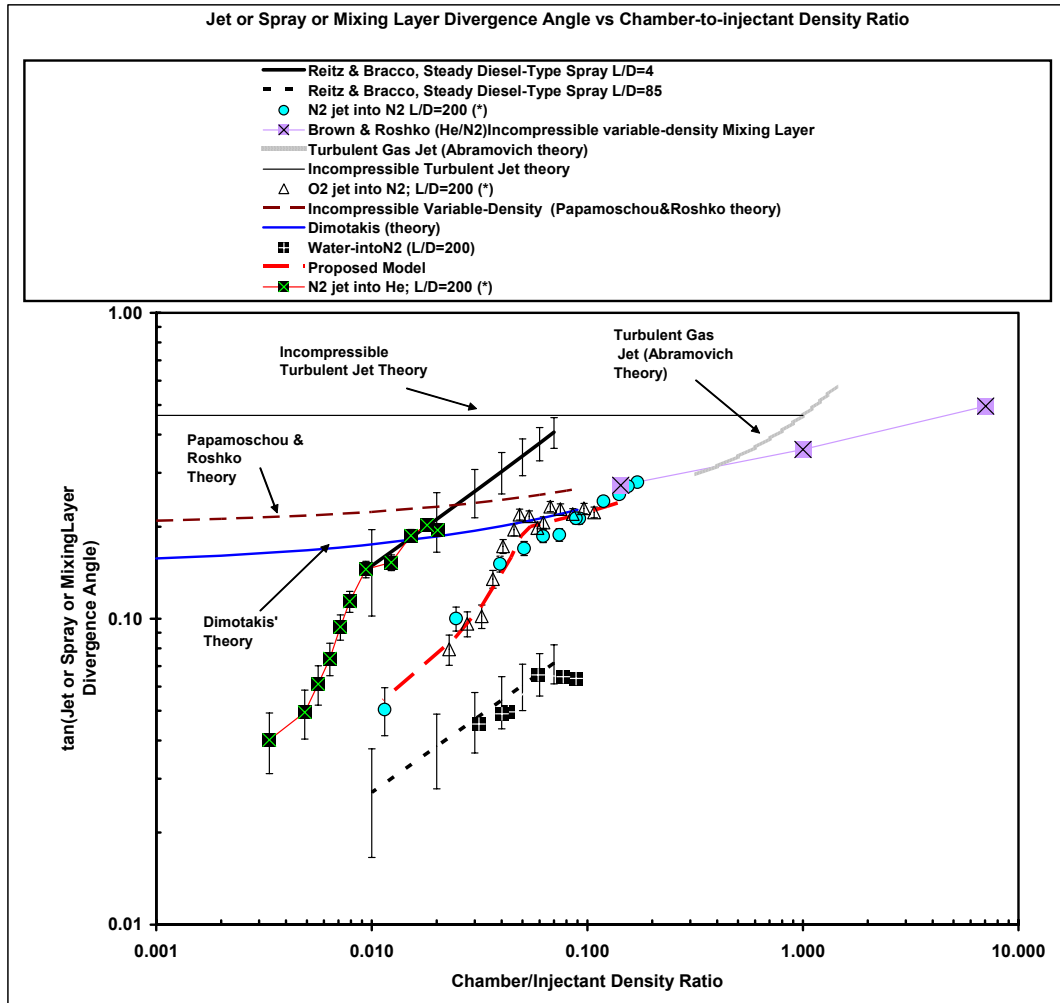


Figure 8. Spreading or growth rate as a tangent of the visual spreading angle versus the chamber-to-injectant density ratio. (*) refers to data taken at AFRL.

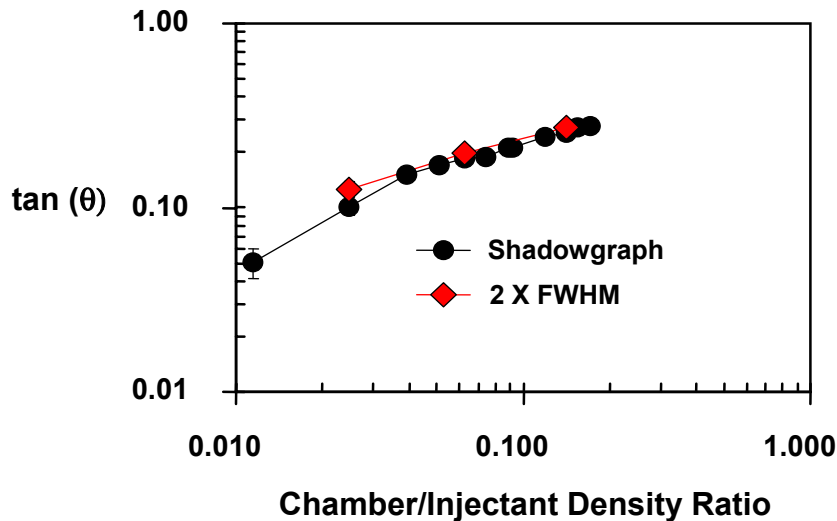


Figure 9: Comparison of the tangent of the spreading angle measured using shadowgraph and Raman techniques using twice the FWHM values.

made using only the information within the first 5.5 mm distance of the injector exit plane. Because both liquid-like and gas-like visual jet behaviors are observed, the growth rate for liquid sprays produced from single-hole nozzles typical of the ones used in diesel engines are also shown. Figure 8 covers a density ratio of four orders of magnitude, from liquid sprays to supersonic mixing layers, a unique and new plot in its own right. To some extent, for comparable measured values, disagreements in this figure can be attributed to differences in the definition of the mixing layer thicknesses and the adopted measurement methods. For detailed discussion of this figure see Chehroudi et al. [11 or 12].

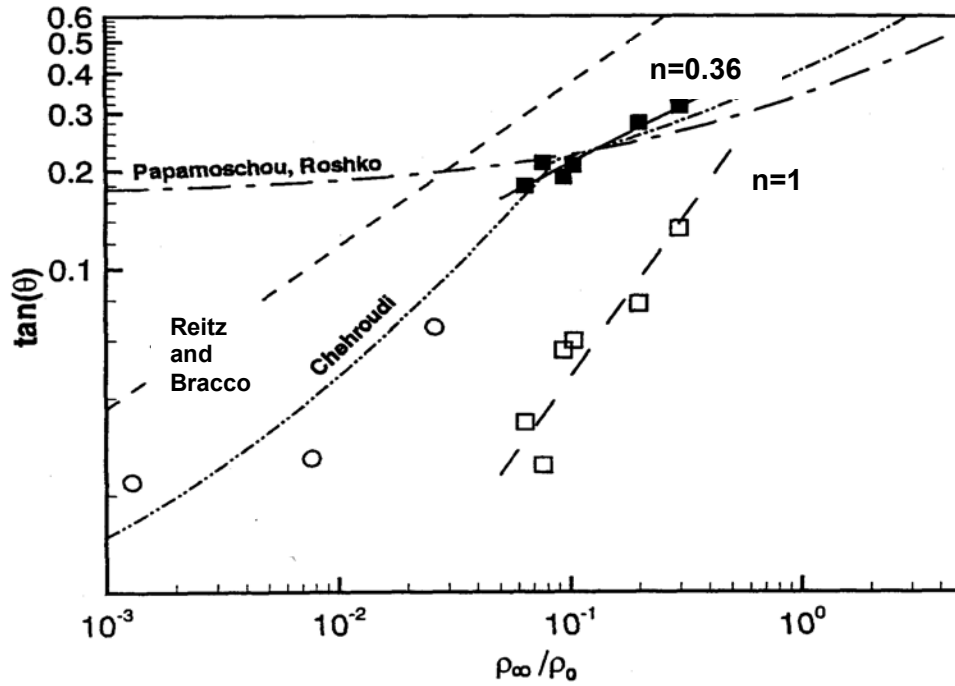


Figure 10: Comparison of the tangent of the spreading angle by Raman techniques using twice the FWHM values and computer simulations (DLR data). Solid squares are for data from x/D of 15 to 32 whereas hollow squares are from x/D of 0.5 to 14. Chehroudi's model is also shown as dash-dot-dot curve. LN_2 into GN_2 with injector $L/D=11.6$. Data from Oswald and Micci [25].

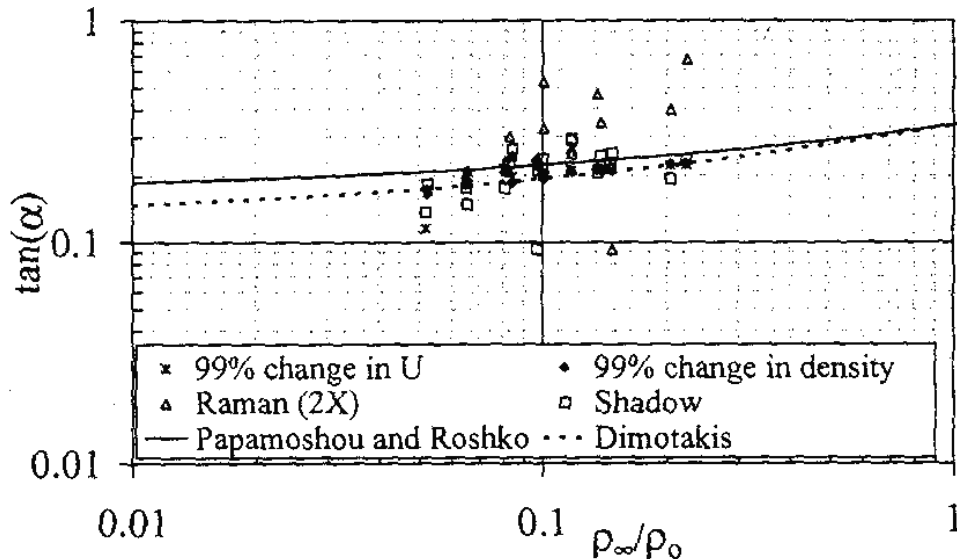


Figure 11: Comparison of the tangent of the spreading angle measured using shadowgraph and Raman techniques using twice the FWHM values and computer simulation (DLR data). LN_2 into GN_2 with injector $L/D=40$. Data by DLR, Branam and Mayer [9]

The important point shown in Chehroudi et al. [12] is that for a range of density ratios in which images show gas-jet like appearance, the experimental data agrees well with the proposed theoretical equation by Dimotakis [24] and closely follows the trend of Brown [22]/Papamoschou and Roshko [23] as shown in Fig. 8. This can be taken as important quantitative evidence that at ambient supercritical pressure and temperature conditions (based on the pure injectant's critical data), the injected jets visually behave like a gas. This was the first time such quantitative evidence had been developed.

Above the critical point, there is a marked disagreement in both magnitude and slope between liquid sprays (at a comparable length-to-diameter ratio of 85) and Chehroudi et al. data (see Fig. 8). The jet appears to go through initial phases of the liquid atomization process, as shown in Fig. 6; however, the cascade of events typical of liquid jet atomization and break-up does not take place. The reason is that, although the jet shows second wind-induced breakup features similar to liquid jets, it fails to reach a full atomization state as chamber pressure (actually, density) is raised. This is because the thermodynamic state approaches the critical point, and consequently both surface tension and heat of vaporization are reduced to near-zero values. Transition into the full liquid atomization regime is therefore inhibited.

Growth rate measurements by Chehroudi et al. using results acquired during the Raman scattering work did not provide the same jet thickness values as those determined by photography. Apparently, as discussed by Brown and Roshko [21], different thickness definitions exist, and one can explore their relationship. Similar attempts showed that within the distances investigated, twice the full width half maximum (FWHM) of the Raman intensity radial profiles, indicating jet density profiles, is equivalent to the thickness values measured through photography. Realization of this relationship was very critical to combine the results from two different methodologies. Figure 9 shows growth rate measured using Raman data in contrast to those determined with shadowgraph images.

These results were subsequently confirmed and extended by DLR researchers through similar measurement techniques. For example, Oswald and Micci [25] showed that when twice the FWHM of the Raman radial intensity profiles are used for x/D between 15 and 32, a good agreement exists between the two laboratories (see the case designated as “ $n=0.36$ ” in Fig. 10). However, there were also disagreements when data for $x/D < 15$ axial locations were considered by Oswald and Micci [25] (see the case identified as “ $n=1.0$ ” in Fig. 10). Note that the data by Chehroudi et al. were all taken near the injector exit up to about x/D of 25. Difficulties in Raman scattering measurements were one important source of observed variability between the results, compounded also by different injector L/D ratios. In Fig. 11, although the growth rates determined by shadowgraphy show good agreements with past results, the Raman data (considering $2 \times$ FWHM) taken by Branam and Mayer does not appear to show a consistent agreement with their shadowgraph images. This is another example where overall difficulties in Raman measurements cause disagreements.

2.1.5 Fractal Analysis

Fractals are intimately connected to the concept of self-similarity (see Mandelbrot [26]). In essence, a similarity transformation involves one or a combination of multiplication by a scale factor, pure translation, and pure rotation. Under such a transformation a geometrical object stays similar to the original or to a preceding stage if repetitively applied. Self-similarity, however, in a strict sense means that if one chooses any point of a geometrical object and locally magnifies, it will look similar to the “whole” object. In nature, however, self-similarity is confined between two sizes (or scales) referred to as inner (the smallest size) and outer cut-offs (the largest size).

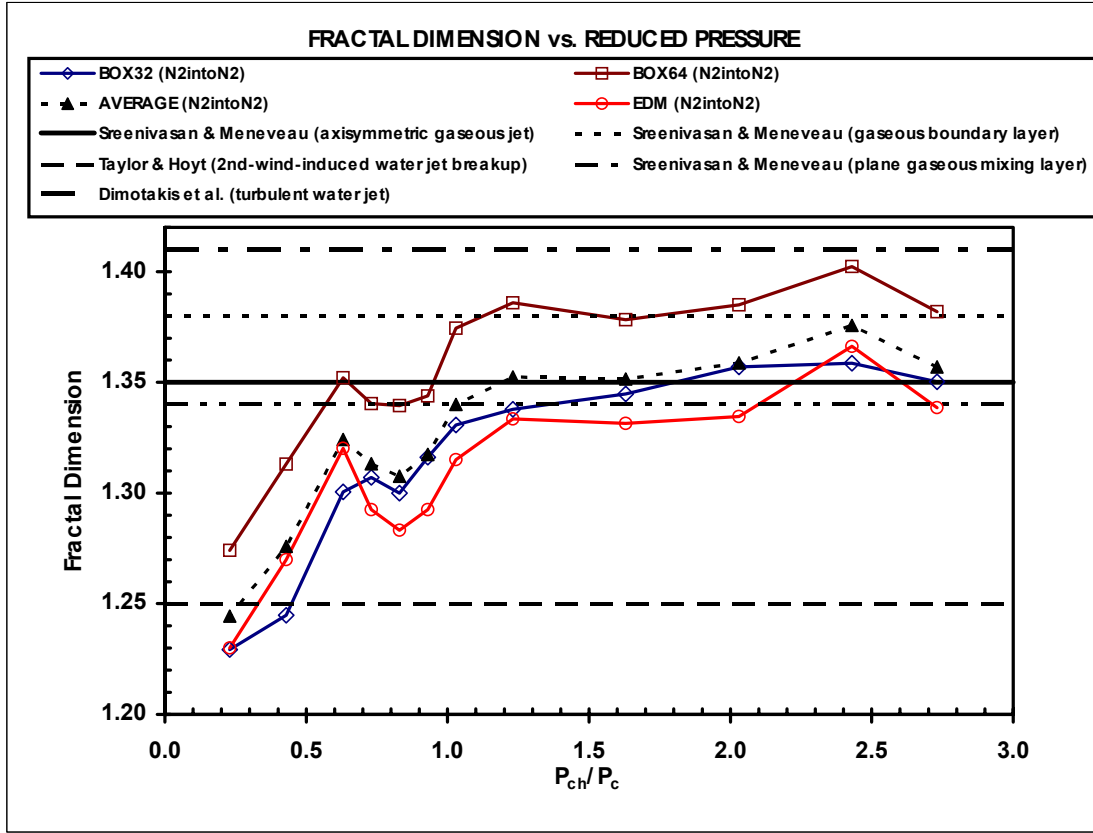


Figure 12. Fractal dimensions of the boundaries of various jets as a function of reduced pressure (chamber pressure divided by the critical pressure of the jet material). Discrete points are data from Chehroudi et al. [20]. Box32, Box64, and EDM are different methods of calculating the fractal dimension, giving an impression of the extent of variability; for details see Chehroudi et al. [20].

The fractal dimension of any curve is between 1 and 2. The more wrinkled and space-filling the curve, the larger the value of the fractal dimension. Natural curves, similar to a cauliflower, are self-similar only to within a narrow range of scales. The objective here is to measure the fractal dimension of the interface of the jets injected into the chamber to see if any pattern is uncovered.

The fractal dimension of jets at various pressures ranging from subcritical to supercritical was calculated and compared to results of other researchers. Reference results were taken from Sreenivasan and Meneveau [27] who measured the fractal dimensions of a variety of turbulent gaseous jets, mixing layers and boundary layers. These results indicate a fractal dimension between 1.33 and 1.38. In addition, the fractal dimensions of a turbulent water jet (Dimotakis et al. [28]) and of a liquid jet in the second wind-induced atomization regime (Taylor and Hoyt [29]) were computed from high-resolution scanned images.

The fractal dimensions from the above reference cases are shown as horizontal lines in Fig. 12. Overlaid on top of these lines are discrete points indicating the fractal dimension of LN₂ jets injected into GN₂ at various chamber pressures. At supercritical chamber pressures, the fractal dimension approaches a value similar to gaseous turbulent jets and mixing layers. As the chamber pressure is decreased, the fractal dimension also decreases. Below $P_r=0.8$, the fractal

dimension rapidly reduces to a value approximately equal to that of a liquid spray in the second wind-induced liquid jet breakup regime.

A more thorough discussion of the above results is found in Chehroudi et al. [20]. The key conclusion here is that the results from fractal analysis complement and extend the imaging data. At supercritical pressures, jets have a fractal dimension similar to turbulent gas jets, and at subcritical pressures, cryogenic jets have a fractal dimension similar to liquid sprays. The transition occurs at about the same pressure as the transition in visual appearance and growth rate.

2.1.6 Raman Measurements

The main purpose of using Raman scattering measurements was to provide more quantitative information and to primarily map the jet density. Using this information, temperatures can be calculated assuming the application of a good equation of state. Intersection of both laser beam and sheet with the jet were considered to map the density field. Difficulties were faced relating to data processing and conversion of measured data to an absolute density value. These complexities stemmed primarily from inadequate information on Raman scattering cross section at near-critical and supercritical conditions. Detailed discussions are available in previous publications by the groups (for examples see Chehroudi et al. [10], Oswald and Schick [8] and also Decker et al. [30]).

For these reasons and for discussion purposes, typical results such as radial density profiles are usually presented in an appropriately normalized fashion. In addition to these density profiles, it should be apparent that growth rate of the jet can also be extracted from these data. Growth rate data from these measurements were previously discussed in the jet growth rate section in this paper. Here the self similarity assessment and centerline density/temperature profiles as a function of axial distances from the jet are discussed.

According to Wygnanski and Fiedler [31], a fully self-preserved velocity field of a turbulent air jet should be observed at an x/D of greater than 40 when Re is near 100,000. So et al. [32] reported self-preservation for x/D larger than about 20 for a binary gas jet at Re of 4300. Although there appear to be some inconsistencies in these criteria, one can see that for near- and supercritical conditions the density radial profile approaches the similarity model curve in Fig. 13(a). Results published by Oswald and Schick [8] also indicate similarity-type profiles for x/D greater than about 10. See examples of two density radial profiles from their work in Fig 13(b).

Figures 14(b) and 14(c) shows normalized centerline profiles of density and temperature acquired by Oswald and Schick [8] at chamber pressure of 4 MPa (near the critical pressure of nitrogen). Note that the density decay becomes faster as the injection temperature is decreased from supercritical (A4 case) to subcritical (C4 case) values. The temperature profile, however, stays flat for up to an approximate x/D of 25 to 30. According to Oswald and Micci [25], the development of the centerline temperature reflects the thermophysical properties of nitrogen specific for the region near its critical point. This is because the injection temperature is below the maximal value of the specific heat (shown as a dashed curve in Fig. 14a), and as the jet heats up, it reaches a value where a large amount of heat can be stored without any noticeable increase in temperature. It appears that the maximum specific heat results in a supercritical fluid behavior similar to a liquid at its boiling point. That is, heat transfer to nitrogen is not increasing its temperature but expanding the fluid (i.e., increasing the specific volume). However, results at higher chamber pressures of 6 MPa did not show features as distinct as those observed for the near-critical case.

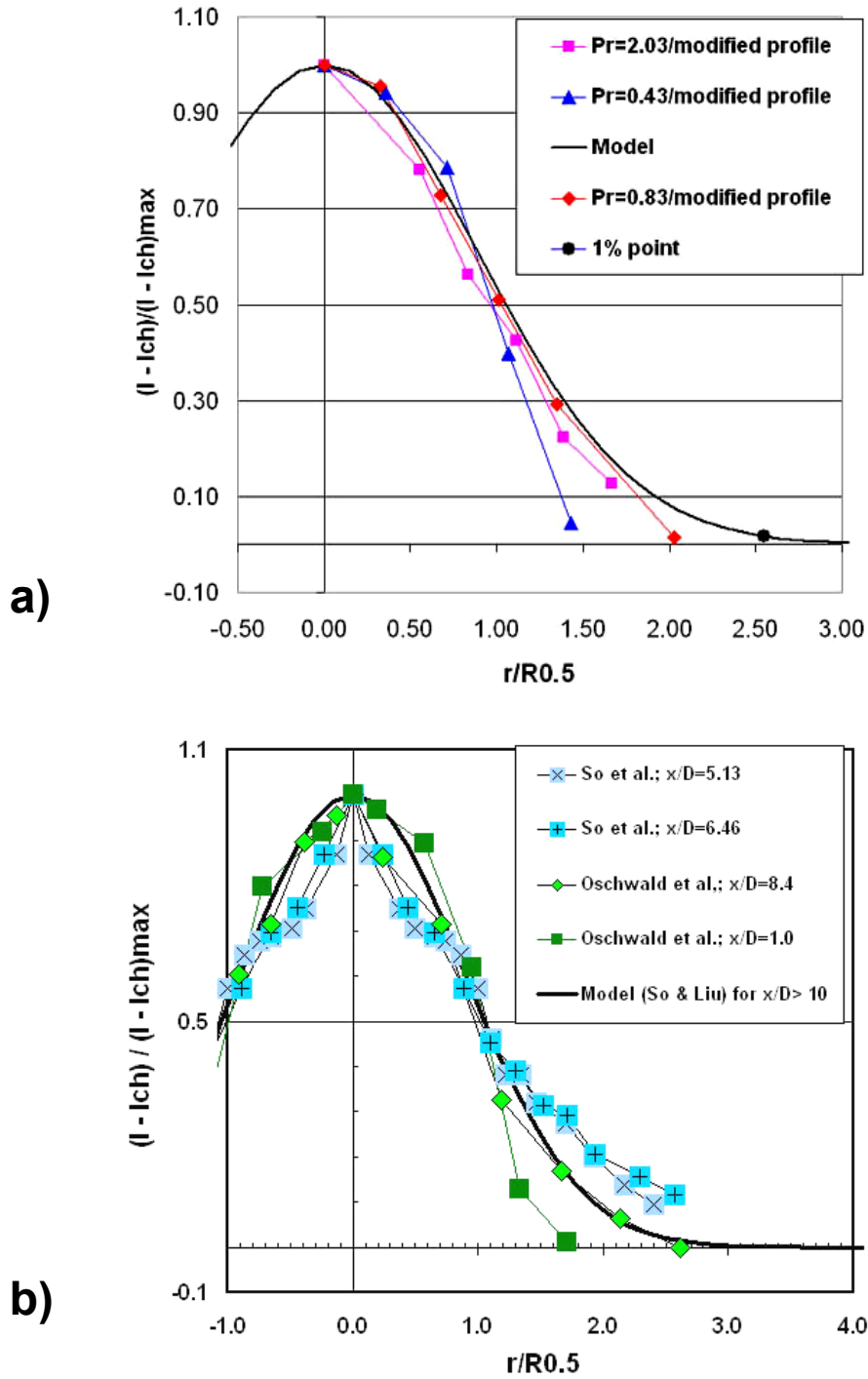


Figure 13: (a) normalized plots of the modified profiles at $x/D=12.2$ under sub- near- and super-critical ambient conditions, Chehroudi et al. (b) similar results for LN_2 into GN_2 injection by Oswald and Schick [8], and gaseous jet experimental data by So et al. [32] The Solid curve is the self-similar model that represents data from gaseous jet injected into gaseous environment. Pr is the reduced pressure.

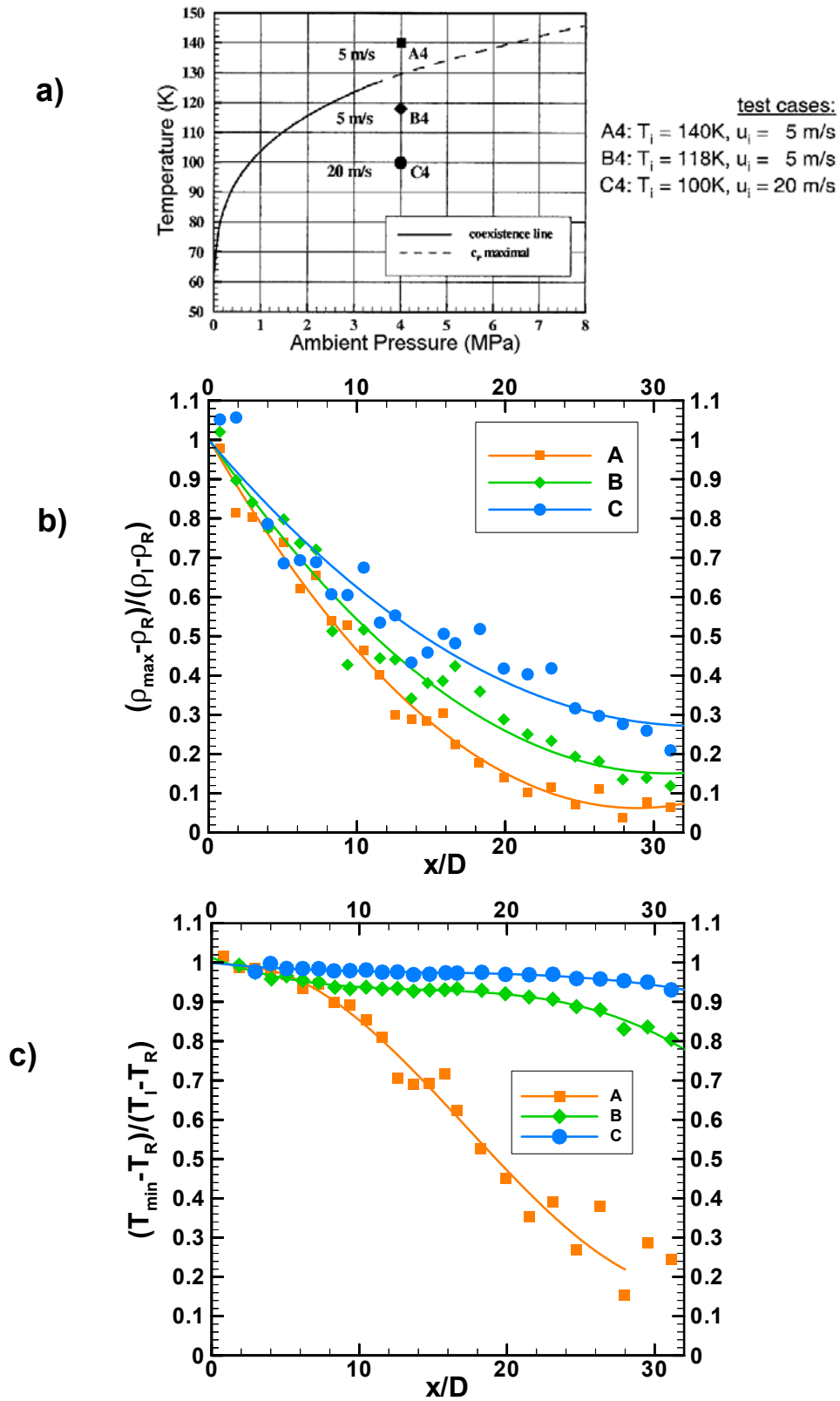


Figure 14: Normalized centerline density and temperature axial profiles of the LN₂ injected into GN₂ at three different injection temperatures and a chamber pressure of 4 MPa (i.e., near critical pressure).

2.1.7 Length scale results

In a coaxially injected rocket combustor, mixing translates into burning efficiency and performance. Mixing is strongly related to the length scales existing within the turbulent shear layer between the O_2 -jet and the annular H_2 -flow. Disintegration of a single LN_2 -jet without annular co-flow has been investigated at 4MPa and 6MPa, 1.17 and 1.76 times the critical pressure of nitrogen. The injection temperature of the nitrogen was near the critical temperature and was injected into N_2 at 298K. Branam and Mayer [9] provided a measure of the length scales by analyzing the images taken by shadowgraphy and named it as the “visible length scale.” They isolated the intensity values of two arbitrarily selected pixels located at a certain distance for 30 to 60 images and then formed the two-point correlation coefficient of these two sets of intensity information. Then, by changing the distance of one of these pixels with respect to the other fixed pixel, they were able to construct a correlation coefficient plot from which a “visible” length scale is calculated. The length scale can be determined through integration, similar to the integral length scale, or by selecting the pixel-to-pixel separation at the 50% correlation value.

The latter approach was selected for this particular analysis due to speed and ease of implementation, accepting a certain level of inaccuracy. Both axial and radial length scales were determined in this manner. Figure 15(b) shows a typical result of the measured geometrically-averaged length scale (average of radial and axial length scales) at an x/d of 10 as a function of radial position. Results from a k - ϵ computational method are also shown. This suggests that the visible length scale is comparable in magnitude to the Taylor length scale as determined by computation.

The ratios of the axial and radial length scales express whether the visible structures are spherical or more ellipsoidal. Both length scales are shown in

Figure 15 (c) and (d) for an injection temperature of 123 K; i.e., injection of N_2 at high density. In the near injector region the axial length scales are much larger than the radial ones. Further downstream the visible structures become more circular. At higher injection temperature (132 K) the asymmetry between L_{rad} and L_{ax} is not as pronounced as at the cold temperature conditions (123 K).

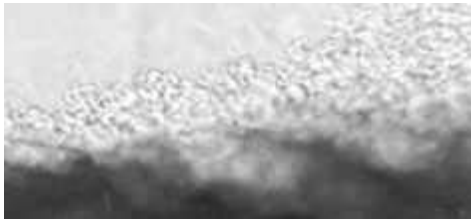


Figure 15(a): Coherent structures in a shadowgraph, 4MPa, $T_{INJ} = 123$ K, $v_{INJ} = 4.9$ m/s, $d_{INJ} = 2.2$ mm

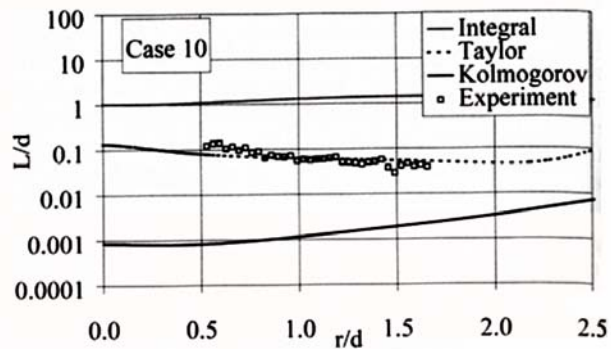


Figure 15(b): Comparison between calculated and experimental length scales L_{int} , L_{Kol} , L_{Tay} at $x/D=10$, 6MPa, 1.9m/s, $T=132$ K.

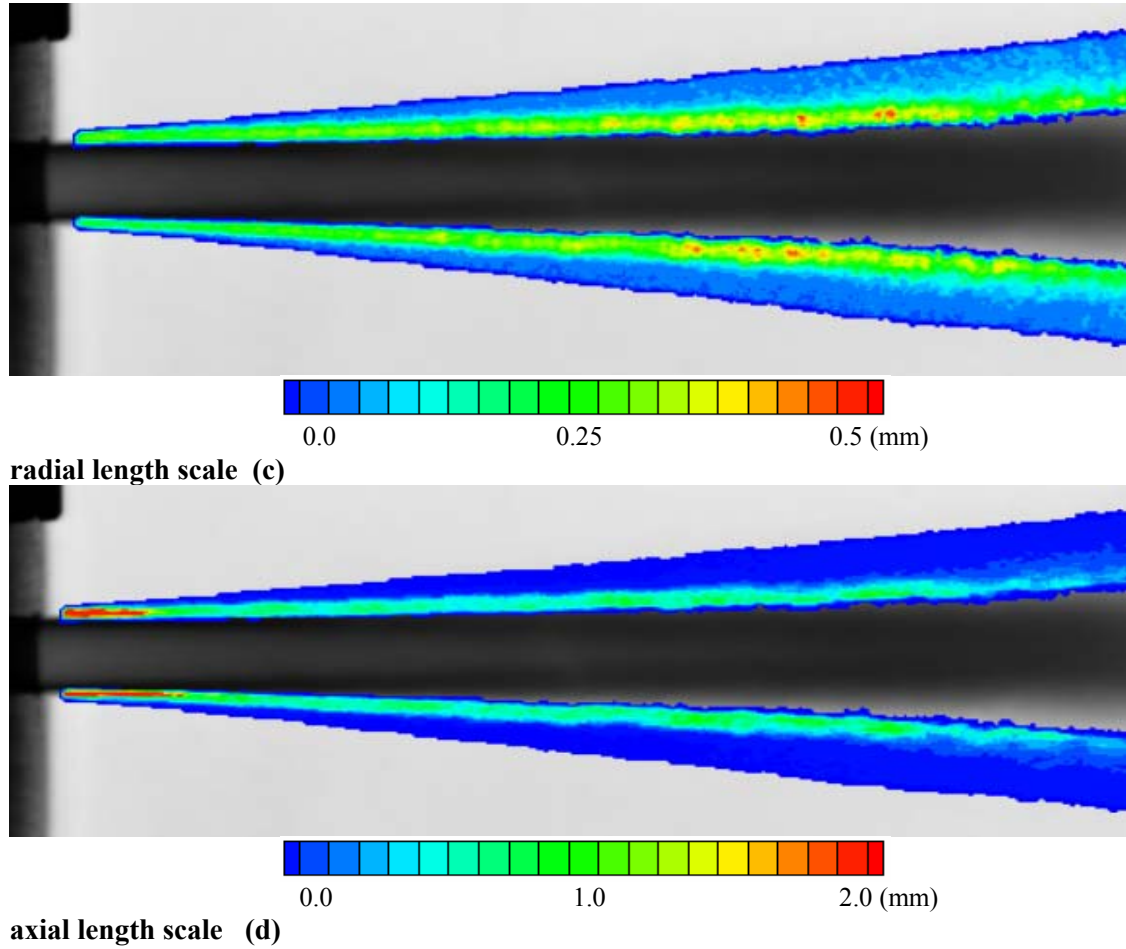


Figure 15 (c) and (d): Experimental length scales for LN₂ into GN₂, 4MPa, 123 K

2.1.8 Interaction with external acoustic fields

Overwhelming evidences gathered by past investigations have attributed combustion instability to a complex interaction of the external acoustic field with the fuel injection processes, thereby leading to incidences of instability in rocket engines. Also, Oefelein and Yang [33] indicated that near-injector processes in the thrust chamber are generally more sensitive to velocity fluctuations parallel to the injector face than normal to it. For this and other reasons, controlled studies have been conducted in the past probing into the effects of acoustic waves on gaseous and liquid jets from a variety of injector hole designs.

Chehroudi et al. [34] used a unique piezo-siren design capable of generating sound waves with a sound power level (SPL) of up to 180 dB. This was used at three chamber pressure conditions of 1.46, 2.48, and 4.86 MPa (Pr of 0.43, 0.73, and 1.43 respectively). The assembly, consisting of an acoustic driver and a high-pressure chamber, forms a cavity that resonates at several frequencies, the strongest being at 2700 and 4800 Hz. They injected LN₂ into GN₂ at room temperature under sub- and supercritical pressures. Three different flow rates were considered, and the nature of the aforementioned interaction was documented via a high-speed imaging system using a CCD camera.

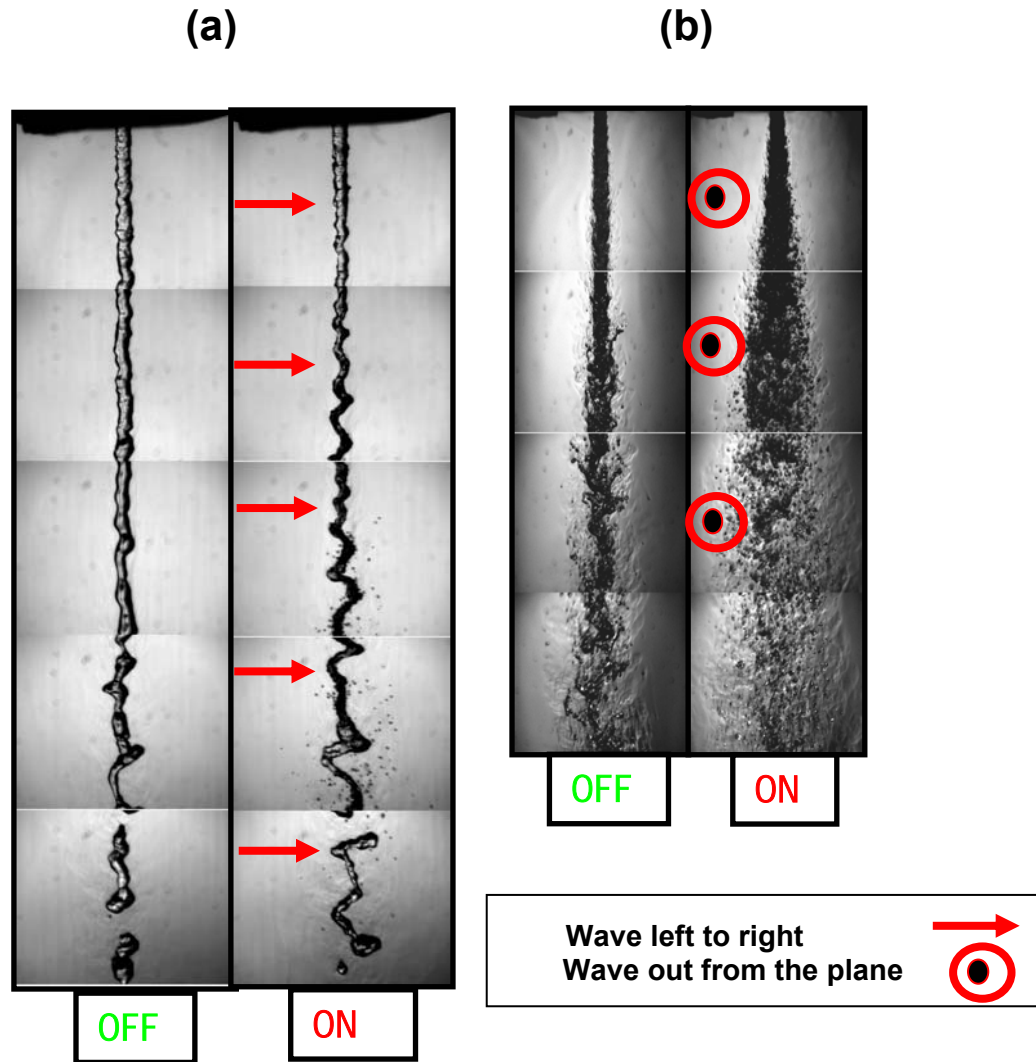


Figure 16. Interaction of acoustic waves with a single LN₂ jet injected into GN₂ at subcritical conditions. “ON” and “OFF” indicate the state of the acoustic driver. (a) front view and (b) side view.

Figure 16 shows some example results from this important study. The acoustic wave constricts the jet in the propagation direction and stretches the jet in the direction perpendicular to the direction of acoustic propagation. Chehroudi et al. [34] found that the impact of the acoustic waves on the jet structure is strongest from low to particularly near-critical chamber pressures and at low injectant flow rates. No significant effects of the acoustic waves are detected at the supercritical chamber pressure. This suggests that engine operation either near the critical point or under a transitory phase passing through the critical point can be troublesome and may lead to, or feed, combustion instabilities in liquid rocket engines.

2.1.9 Phenomenological model of the jet growth rate

Using the data collected on the growth of a cryogenic jet, a phenomenological model for the growth rate has been developed. Complete details about the development of this equation are given in Chehroudi et al. [20]. The physical reasoning motivating the equation is outlined below. It was noticed that previous expressions for the growth rate of liquid sprays and of turbulent jets have a remarkably similar form. Reitz and Bracco [15] proposed that the growth rate of an isothermal steady liquid spray could be expressed as,

$$\theta \approx 0.27[0 + (\rho_g / \rho_l)^{0.5}].$$

The first term in the bracket is the number zero to contrast with other equations discussed next. Similarly, Papamoschou and Roshko [23] suggested the following form for incompressible, but variable-density, turbulent gaseous jets:

$$\theta = 0.212[1 + (\rho_g / \rho_l)^{0.5}].$$

The similarity in the form of these equations suggests the potential for a link between the two. Imagine a jet that is being injected into a subcritical pressure environment similar to the ones shown in Fig. 6. Clearly there are drops and ligaments, testifying to the existence of surface tension. Also, evidence of a phase change is seen. Hence, one appropriate characteristic time of the problem (at subcritical, $P_r < 1$) is the “bulge” formation/separation time (τ_b) on the interface of the turbulent liquid jet. This time characterizes the formation and separation event of bulges from the liquid jet producing isolated ligaments and drops. Tseng et al. [35] suggests that this time is equal to $(\rho_l L^3 / \sigma)^{1/2}$ for the primary breakup of turbulent liquid jets where ρ_l , L , and σ are liquid density, characteristic dimensions of turbulent eddies, and surface tension, respectively. The second relevant characteristic time (at subcritical) is the gasification time (τ_g). Here, an estimate of this time is calculated through the so-called D-squared law for drops to be equal to D^2/K where D and K are drop diameter and vaporization constant, respectively. In addition, we also propose the following hypothesis. If the aforementioned characteristic times (calculated for appropriate length scales) are nearly equal in magnitude, then the interface bulges are not able to separate as unattached entities from the jet interface to form ligaments and drops, because they are gasified as fast as they desire to be detached. Here, this is defined as the onset of the gas-jet like behavior. Therefore, the transition between liquid-like and gas-like behavior would be governed by finding the point at which these time scales are approximately equal. This is suggested by the comb-like structures seen in Fig 6(b).

Using the above physical models, an equation was proposed for the N_2/N_2 system as

$\theta = 0.27[(\tau_b / (\tau_b + \tau_g)) + (\rho_g / \rho_l)^{0.5}]$. In the limit, when $\tau_g \gg \tau_b$ and $\tau_g \rightarrow \infty$, this equation collapses to the isothermal liquid spray case. This equation agrees well with the current data at subcritical pressures for $\tau_b / (\tau_b + \tau_g) < 0.5$. A constant value of 0.5 was used to predict the spreading rate for higher pressures, including supercritical pressures.

For injection of N_2 into N_2 , the characteristic time ratio, $\tau_b / (\tau_b + \tau_g)$, was calculated from experimental measurements of bulge and droplet sizes and calculations of the relevant properties. For N_2 injection into other gases, however, reliable information about the mixture properties at the interface, particularly the surface tension, prevents such a calculation from being performed. To model these cases, it is hypothesized that the characteristic time ratio is a dominant function of the density ratio; i.e., $\tau_b / (\tau_b + \tau_g) = F(\rho_g / \rho_l)$. Brown and Roshko [21] indicate that this hypothesis is reasonable, because at low Mach numbers there is no distinction between mixing layers where the two streams have different molecular weights, temperatures, or compressibility

effects. Measurements and calculations of $\tau_b / (\tau_b + \tau_g)$ provides the shape of the function F for the N_2/N_2 system and is provided as a plot in Chehroudi et al. [20]. A curve fit of that plot gives

$$F(\rho_g / \rho_l) = 5.325 (\rho_g / \rho_l) + 0.0288 \quad \text{when } \rho_g / \rho_l < 0.0885$$

$$= 0.5 \quad \text{when } \rho_g / \rho_l \geq 0.0885$$

It was found that the same function, F, calculated from measurements of the N_2/N_2 system could be made to work for other cases, provided that a case-dependant transformation was made to the density ratio at which F is evaluated. The final form of the equation thus arrived at is

$$\theta = 0.27[F(x(\rho_g / \rho_l)) + (\rho_g / \rho_l)^{0.5}],$$

where, $x=1.0$ for N_2 -into- N_2 , $x=0.2$ for N_2 -into-He, and $x=1.2$ for N_2 -into-Ar.

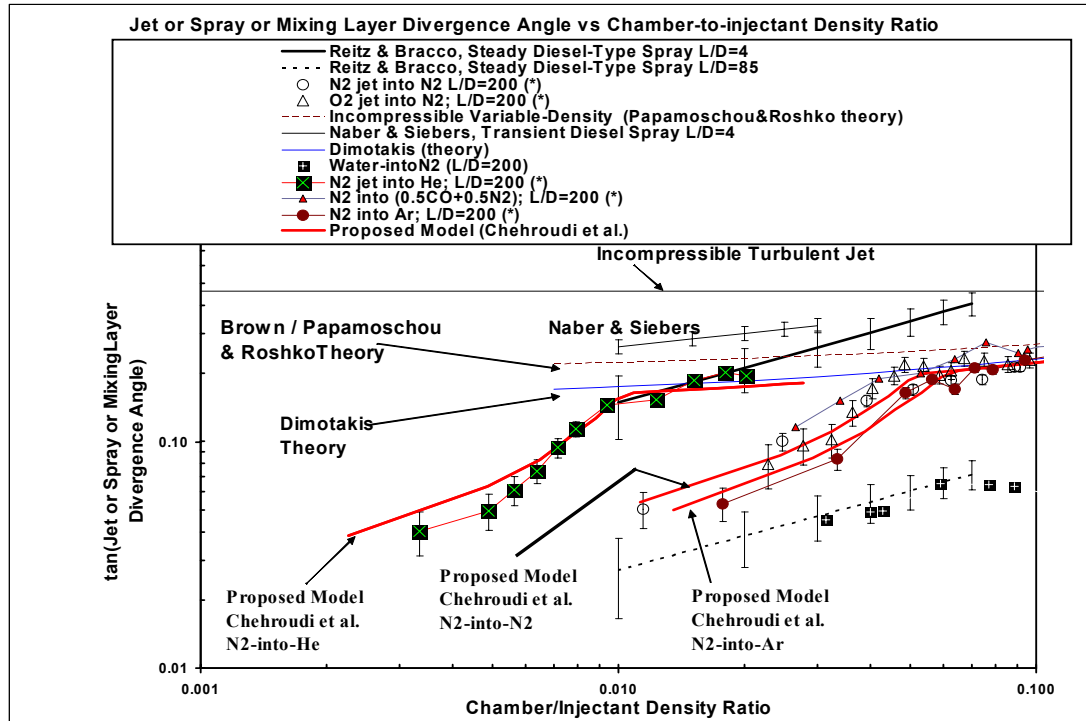


Figure 17. Comparison of the proposed growth rate model with experimental data.

In other words, the same functional form of the characteristic time ratio, $\tau_b / (\tau_b + \tau_g) = F(\rho_g / \rho_l)$, for the N_2 -into- N_2 case is used but with a density-ratio coordinate transformation. The quality of the agreement with experimental data is demonstrated in Fig. 17. Hence there are no major changes in the form of the proposed model equation, even for an extreme arrangement such as injection of N_2 into He. However, an observation is made here. The factor $x=0.2$ in the N_2 -into-He case is comparable to the molecular weight ratio of He to N_2 of 0.14, while the factor $x=1.2$ in the N_2 -into-Ar case is comparable to the molecular weight ratio of 1.42. This also suggests the dominant effect of the density ratio parameter between the cases.

2.2 Coaxial jets

2.2.1 Shadowgraphy

The change of coaxial injection atomization phenomenology when increasing the pressure from sub- to supercritical conditions has clearly been confirmed in cold-flow tests with simulant fluids

LN₂ and gaseous Helium (GHe), see Telaar et al. [36]. In these tests a coaxial injector with an inner diameter $d_{\text{LN}_2} = 1.9$ mm for the nitrogen flow and an annular slit width 0.2mm with an outer diameter of 2.8mm for helium has been used. Two examples of flow visualizations using shadowgraphy of the near injector region are shown in Figure 18. The change in the atomization mechanism at reduced surface tension is evident: spray formation at low pressure and turbulent mixing of dense and light fluid components at supercritical pressure conditions. The injection temperature of nitrogen was 97 K, and the ambient pressure was A: 1MPa and B: 6MPa. The critical mixing temperature of He/N₂ is 125.7K. Thus in the mixing layer between LN₂ and He, transcritical zones may exist. The boundary of the LN₂-jet as shown by the shadowgraphs is assumed to be the layer which reaches the critical mixing temperature. The effect of surface tension compared to shear forces appears to be negligible in the high-pressure case.

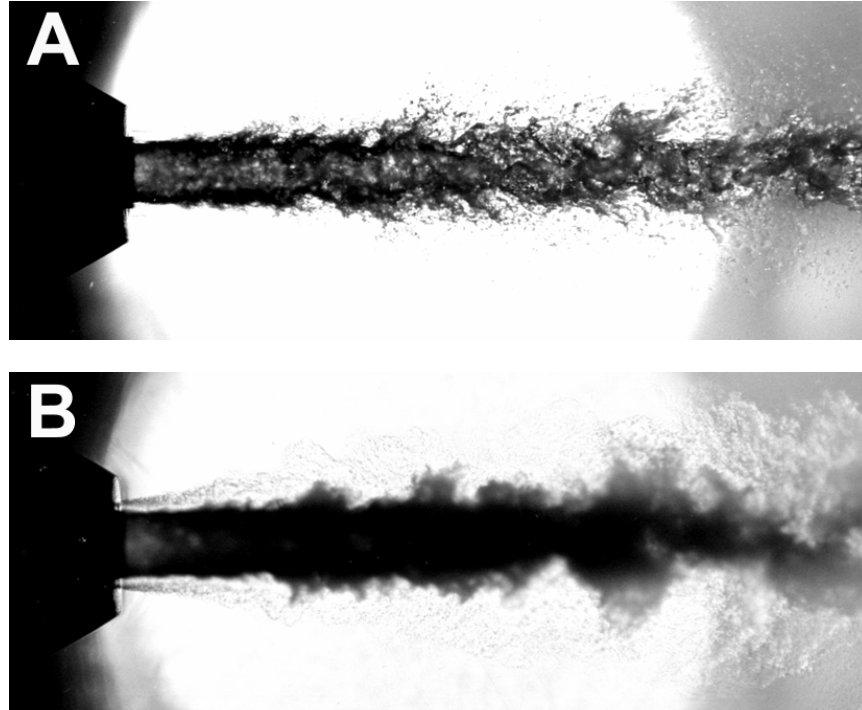


Figure 18. Binary liquid N₂/GHe system at A: 1.0 MPa, B: 6.0 MPa. $d_{\text{LN}_2} = 1.9$ mm, $v_{\text{LN}_2} = 5$ m/s, $v_{\text{He}} = 100$ m/s, $T_{\text{LN}_2} = 97$ K, $T_{\text{He}} = 280$ K (from Mayer and Smith [39])

2.2.2 Raman measurements

The potential of spontaneous Raman scattering for quantitative density determination in cryogenic high-density jets has been demonstrated in the single-N₂-jet investigations discussed in a previous section. Application of Raman scattering is realizable under such conditions, as during the inelastic Raman scattering process there is energy exchange between the exciting photon and the rotational/vibrational modes of the molecule. The Raman-signal is frequency shifted by an amount specific for the molecule of investigation.

In a mixture of N₂ and H₂ the Raman signals of N₂ and H₂ are generated at two different wavelengths. Thus, using appropriate filter techniques, the signals of both species can be analyzed independently and the partial densities of both species can be determined.

This diagnostic method has been used to investigate the disintegration of a cryogenic N₂-jet and the mixing of H₂ and N₂ for coaxial LN₂/H₂-injection at supercritical nitrogen pressures, see

Oschwald et al. [37]. The test matrix is listed in Table 2. During all tests, the fluids were injected into a flow channel filled with N_2 at near ambient temperature, and the pressure was 4MPa ($P/P_{crit}=1.17$). Comparison tests have been performed with co-flow (cases D4, E4, F4) and without co-flow (A4, B4) of hydrogen at identical injection conditions for LN_2 . The temperature chosen for nitrogen was above (A4, D4) and below (B4, E4, F4) the pseudo-boiling-temperature (see Figure 19). At the pseudo-boiling temperature the specific heat and the density variation with temperature $\frac{\partial \rho}{\partial T}$ show extrema (see Figure 4). The strong expansion of nitrogen with increasing temperature at the pseudo-boiling temperature reflects a liquid-like behavior, although the pressure is above the critical pressure of nitrogen. The transition of a fluid from the liquid phase to the gas phase due to boiling is associated with a significant decrease of the density.

Table 2: Injection conditions for Raman scattering tests

	test case	v_{N_2} [m/s]	T_{N_2} [K]	v_{H_2} [m/s]	T_{H_2} [K]
single N_2 -jet	A4	5	140	-	-
	B4	5	118	-	-
coaxial N_2/H_2 -jet	D4	5	140	60	270
	E4	5	118	120	270
	F4	5	118	60	270

Typical radial density profiles for nitrogen without H_2 -coflow (case A4) are shown in Figure 20. Similar plots for nitrogen and hydrogen in a coaxial injection configuration are outlined in Fig. 21. (The decrease of the measured densities for large r/D is due to the refraction of the laser-beam at the density gradients at the N_2/LN_2 or H_2/LN_2 interfaces.)

These profiles have been determined for a range of various downstream locations from the injector. From these data the two-dimensional species distribution can be reconstructed. For test case D4 the distribution of H_2 is shown in Figure 22.

The maximum of the radial density distribution has been plotted as functions of distance x/D from the injector (see Figs. 23, 24, 25, and 26). This is used as a measure of the evolution of atomization of the LN_2 -jet downstream of the injector and the mixing of H_2 and N_2 . With co-flow the nitrogen density reduces much faster from its injection value ρ_{INJ} to its value ρ_∞ for large x/d , which corresponds to complete mixing of the jet within the background gas. The distances $x_{1/2}$ correspond to a nitrogen density decrease of 50% ($\rho(x_{1/2}) = \rho_\infty + 0.5(\rho_{INJ} - \rho_\infty)$) and are listed in Table 3. The increased atomization efficiency of the N_2 -jet with the co-flowing H_2 is clearly seen when comparing the $x_{1/2}$ -value of test cases A4 and D4. Comparisons can be made between the test with the N_2 -injection temperature above the pseudo-boiling temperature (test D4, $T_{N_2}=140K$), with those with injection temperature below the pseudo-boiling temperature (tests E4 and F4, $T_{N_2}=118K$).

Comparisons indicate that a jet above the pseudo-boiling temperature has a shorter decay length than a jet with a temperature below the pseudo-boiling temperature. In both cases the injected N_2 is in the supercritical state. However, as can be seen in Figure 4, nitrogen above the pseudo-boiling temperature has a gas-like density, whereas N_2 below this temperature has a much higher, liquid-like density. Thus the jet has more inertia to resist the shear forces from the annular H_2 -jet. The effect of higher H_2 -velocity is not as pronounced as this N_2 -density effect, as can be seen when comparing the decay-lengths of test case E4 ($v_{H_2} = 120$ m/s) and F4 ($v_{H_2} = 60$ m/s).

Although one may expect a decrease in H_2 -density downstream of the injector, due to the H_2 mixed with N_2 , the Raman measurements show an increase of the H_2 -density. This effect is significantly more pronounced for test case E4 ($T_{N_2} = 118$ K) than in test case D4 ($T_{N_2} = 140$ K). The increase of the hydrogen density is therefore attributed to the heat transfer from hydrogen to the cryogenic nitrogen and diffusion of hydrogen into the dense nitrogen, resulting in decreasing hydrogen temperature and increasing density.

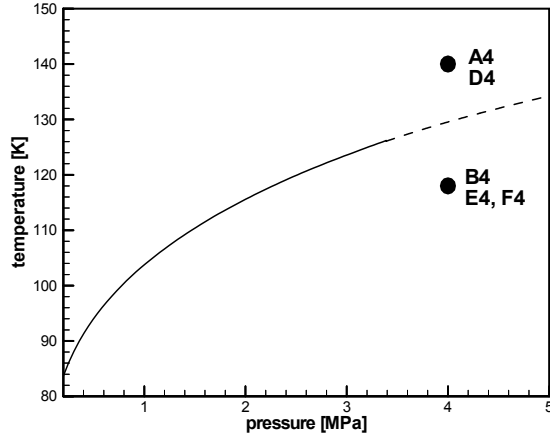


Figure 19. Density and specific heat of N_2 as a function of temperature. Dashed line corresponds to the pseudo-boiling line (c_p is maximum).

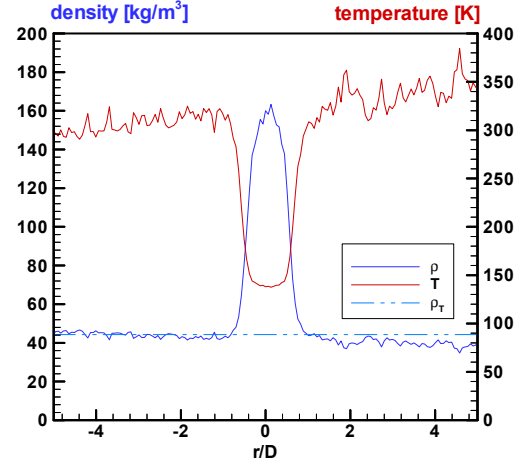


Figure 20. Radial N_2 -density profile for test case A4, 2mm ($x/D=1.05$) downstream of the injector exit.

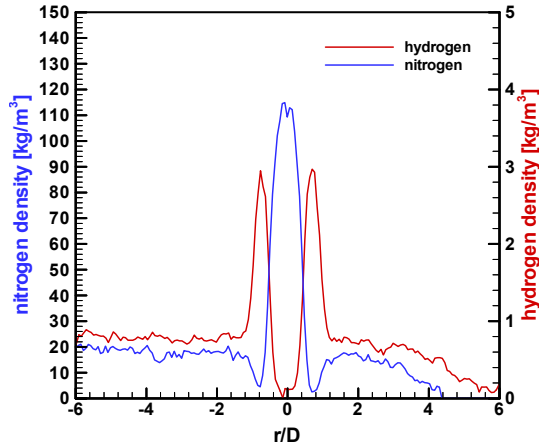


Figure 21. Radial N_2 - and H_2 -density profiles for coaxial N_2/ H_2 -injection for test case D4, 2mm ($x/D=1.05$) downstream the injector exit.

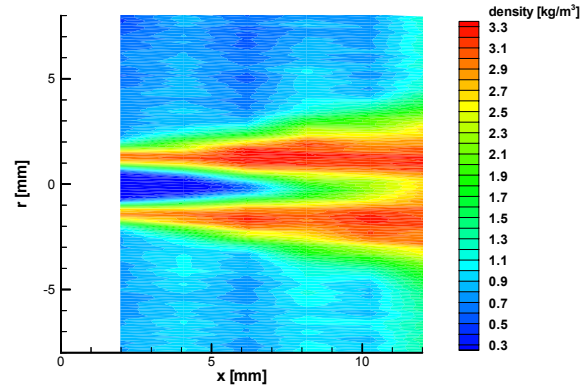


Figure 22. H_2 -density for coaxial injection of N_2 and H_2 for test case D4 ($T_{N_2} = 140$ K, $T_{H_2} = 270$ K).

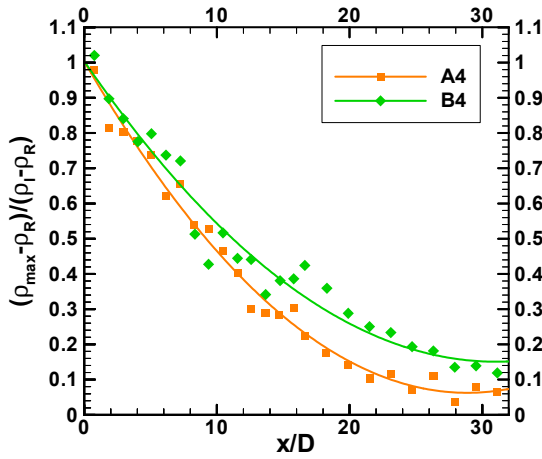


Figure 23. Evolution of the maximum nitrogen density downstream of the injector for test cases A4 and B4.

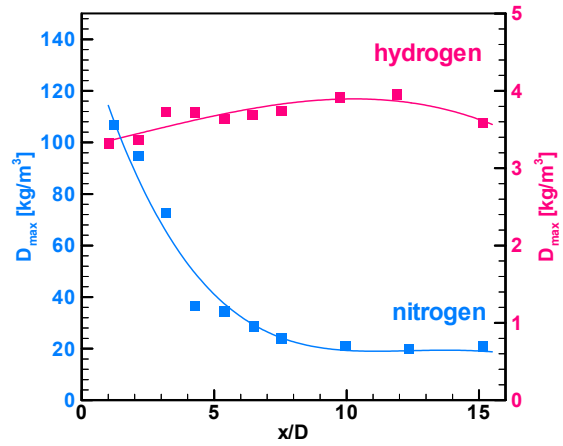


Figure 24. Evolution of the maximum nitrogen and hydrogen density downstream of the injector for test case D4.

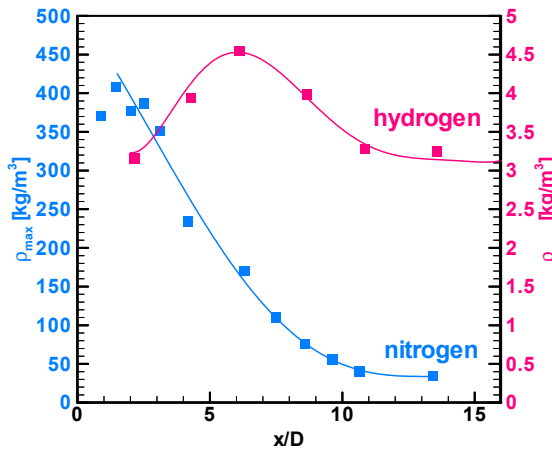


Figure 25. Evolution of the maximum nitrogen and hydrogen density downstream of the injector for test case E4.

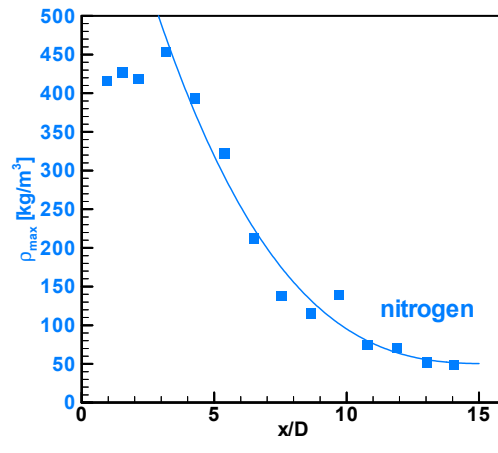


Figure 26. Evolution of the maximum nitrogen and hydrogen density downstream of the injector for test case F4

Table 3: Distance where nitrogen density has decayed to 50% of its injection value.

test case	A4	B4	D4	E4	F4
$x_{1/2}/D$	9	11	3	5.5	6

2.2.3 Interaction with external acoustic fields

In a systematic study, Chehroudi et al. [38] designed a coaxial injector based on their single jet injector design and studies to take advantage of their earlier findings. In their initial results, they investigated the effects of the external acoustic waves on the visual structure of the jet by shadowgraphy. Evidences indicate that the warmer coflow GN2 in the annular region of the

injector affected the thermodynamic condition of the LN2 jet near the inner wall surface, reducing the jet initial visual diameter, particularly at higher gaseous coflow rates. Dramatic effects of the periodic transverse acoustic waves can be seen to impose a sinusoidal shape to the jet appearance, see Fig. 27. The wavelength of this wavy-shaped structure, λ_{Super} is established by the acoustic-induced transverse deflection of the jet, considering the fact that the jet exists in the velocity antinode of the acoustic field. Injector modifications to provide more realistic flow conditions and collection of more data are needed to fully map and explain these initially-observed and interesting interactions. Further results may shed light on injector-acoustic field interactions in the context of combustion instability in engines.

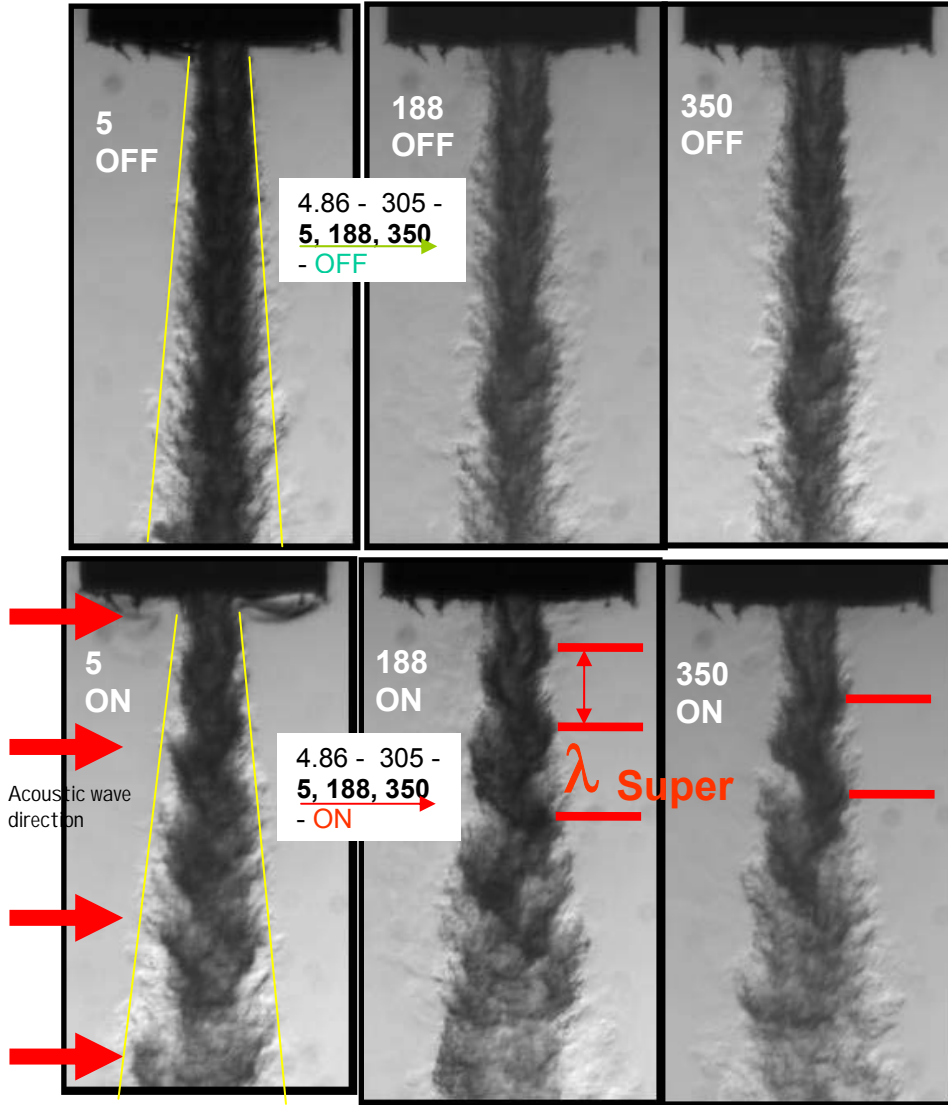


Figure 27. Effects of the acoustic waves on a coaxial injector under supercritical condition at a core flowrate of 300 mg/s and three different coflow rates of 5, 188, 350 mg/s. Code: ChamberPressure(MPa) - Coreflow(mg/s) - Coflow(mg/s), Coflow(mg/s), Coflow(mg/s) - AcousticField(ON/OFF).

3 Combustion studies

It has recently been demonstrated that combustion, and more specifically, reaction rate-related processes such as atomization, mixing and vaporization behave very differently at conditions near and above the thermodynamic critical point of the injectants (Yang [39], Mayer and Smith[40], Mayer and Tamura[41], and Mayer et al. [42]). It is therefore essential to characterize cryogenic injection and combustion at supercritical pressure conditions experimentally in order to build a database to validate models and numerical tools for the simulation of rocket combustion chamber processes.

At the test bench P8 in Lampoldshausen, injection of liquid oxygen (LOX) and H_2 can be investigated at thermophysical conditions representative for high-pressure rocket combustors in hot-fire combustion testing. A modular combustion chamber is operated with a single injector head and is dedicated for quantitative and qualitative investigations of supercritical injection and combustion studies. A combustion chamber module with optical access enables the application of non-intrusive optical diagnostic techniques (see Fig. 28). Shadowgraphy and imaging of the flame emission are applied for qualitative characterization of the near injector process. Spectroscopic methods are used for non-intrusive quantitative thermometry within the combustion chamber volume.

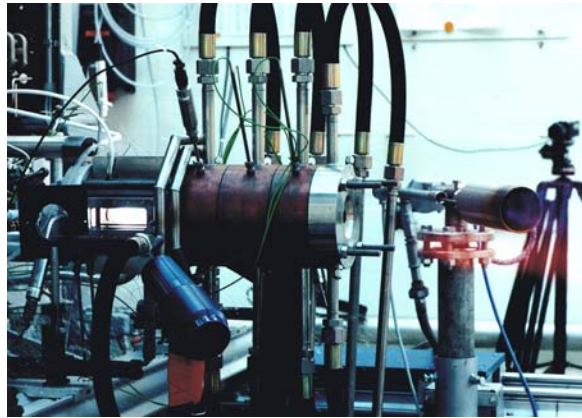


Figure 28. Windowed combustion chamber "C" with module for optical access at test bench P8

3.1 Shadowgraphy

Similar to cold flow investigations, the position and value of refractive index gradients in a combustive flow can be visualized using shadowgraphy. The method is well developed, in general easy to apply and nevertheless delivers important information about the spatial organization of the flow field. A critical experimental point with the application to high pressure H_2/O_2 -flames is the suppression of the intensive flame emission, which may interfere with the radiation from the light source used for shadowgraphy.

In Figure 29(a) a shadowgraph of the O_2 -jet is shown under hot fire conditions at a chamber pressure (1.5 MPa) clearly below the critical O_2 -pressure (5.04 MPa). The LOX-jet is atomized, forming a spray comparable to the flow pattern visualized from cold flow studies. Ligaments are detached from the LOX-jet surface, which form droplets and finally evaporate. The droplet number density is much smaller as compared to cold flow conditions, a fact that is due to the rapid vaporization of the small droplets in the burning spray.

At supercritical pressure with respect to the propellants, the mixture may initially be below the critical mixing temperature. However, due to convective transport of hot gases from the reaction zone to the O₂-jet surface, the local temperature will increase and the jet enters the supercritical regime. A shadowgraph of the O₂-jet at supercritical burning conditions at a pressure of 10 MPa is shown in Figure 29(b). Droplets are no longer visible, and the O₂-jet stringy or thread-like structures which typically develop and grow no longer detach but rapidly dissolve. Under supercritical conditions the flow is dominated by turbulent gas-like mixing. The boundary between the dense, cryogenic O₂-core and the gaseous co-flow appears as a steady transition, in contrast to the well-defined boundary between the liquid O₂-jet and the annular gas-flow at subcritical pressures.

Further downstream at supercritical conditions, the visualization shows a compact jet-core, and oscillations of the O₂-jet are visible; whereas at subcritical pressure the jet already disintegrates into individual droplets. A zoom of the region 60-72mm downstream of the injector, as shown in Figure 30, demonstrates the remarkable difference between sub- and supercritical atomization under hot fire conditions. At subcritical pressure a spray of LOX-droplets and ligaments can be seen, whereas at supercritical conditions the jet disintegrates into O₂-clumps of a size much larger than the typical liquid entities observed in the subcritical case.

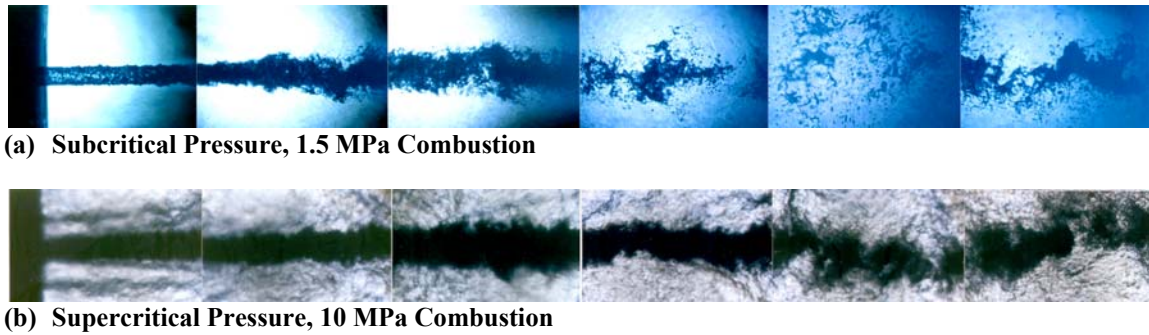


Figure 29: LOX-jet at subcritical (a) and supercritical (b) pressure conditions (from Mayer and Tamura. [43])

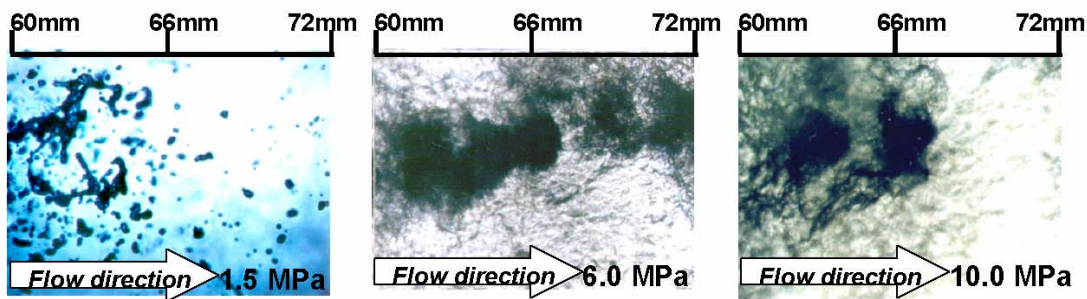


Figure 30: Visualization of O₂-jet disintegration with varying chamber pressure (Mayer and Smith [39])

3.2 Quantitative studies

3.2.1 OH fluorescence

Information on the location and structure of the reaction zones in the LOX/ H₂ flames is obtained by recording the flame emission in appropriate wavelength regions. A spectrum of an H₂/O₂-flame at 6 MPa is shown in Figure 31. At approximately 310nm, a distinct peak exists, which originates from chemiluminescence from the OH radical and indicates chemical activity within the flow. At wavelengths above 400nm the flame emits a broad continuum which shows some local maxima. These maxima correspond to overtone transitions of the reaction product water. At ambient pressure, H₂/O₂-flames show virtually no emission in the optical wavelength region, and only emission of the OH radical in the UV can be detected. With increasing pressure H₂O-emission is increasing in a non-linear fashion, and the spectral density of the H₂O-emission can become higher than that of the OH-emission. By application of suitable band-filters corresponding to the wavelength region $\lambda=300\text{-}310\text{nm}$ or a high pass filter for $\lambda>500\text{nm}$, the emission of the OH radical or the reaction product H₂O can be selectively detected.

Detecting the OH-emission with a camera is a line-of-sight method. By application of a deconvolution technique utilizing the Abel's transform, a planar distribution of the flame emission in plane through the axis of symmetry can be reconstructed from a rotationally symmetric flame. The results for a temporally averaged deconvoluted OH emission image at 6 MPa chamber pressure is shown in Figure 32 in the flow region immediately downstream of the coaxial injector. The flame is forming a conical sheet between the O₂-jet and the annular H₂-flow. OH-emission is clearly seen extending from the LOX injector post, thus confirming a stabilized flame due to the recirculation zone and flame anchoring at the LOX-post. For comparison, a shadowgraph of the flow is shown in the upper half of Figure 32. It can be seen that the flame intensity is highest very close to the O₂-core.

Results for the flame emission in the wavelength regions for OH and H₂O are given in Figure 33 and 34 respectively. OH- as well as H₂O-emission can be detected starting at the O₂ injector post. Local emission is strongest for both species near to the injector and decreases downstream. The images show a somewhat larger extension in radial direction for the H₂O-emission.

From temporally resolved OH-images, length scales have been determined by the spatial correlation of OH-emission in the flow by Ivancic and Mayer [44]. In Fig. 35 these length scales are compared with results from numerical simulations. The integral and Kolmogorov length scales as calculated using AS3D are shown from the injector faceplate to $x=30\text{mm}$ downstream. The radial location has been chosen where the OH-emission is maximum. The experimental length scales lie between the integral and the Kolmogorov length scale of simulation but closer to the integral length scale.

From the deconvoluted OH-images, the downstream evolution of the thickness of the OH-zone can be determined. The thickness is increasing very rapidly after its formation at the O₂-post. At 30mm downstream of the injector, the thickness is approximately 4mm, which is about four times higher than the measured length scales within the reaction shear layer. However, it is important to remember that the determination of the width of the OH-zone is based on an average of several images and with a vibrating test specimen.

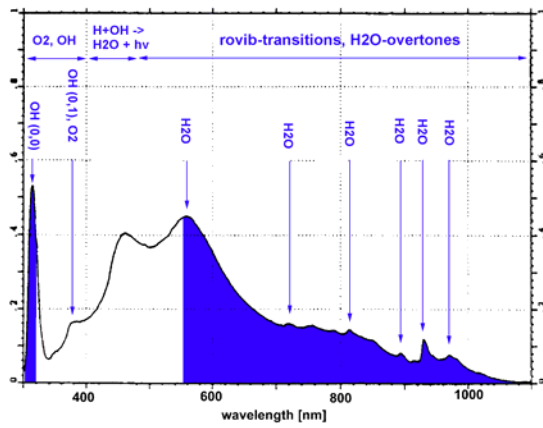


Figure 31. O₂/ H₂-flame spectra at 6 MPa (Ref. [42])

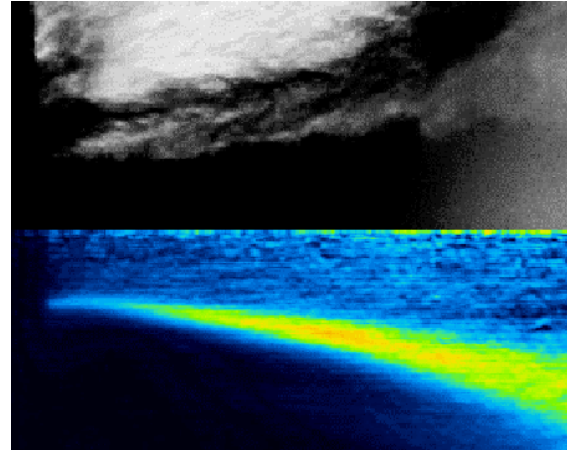


Figure 32. Shadowgraph (top) and OH flame-emission (bottom) of the near injector region.

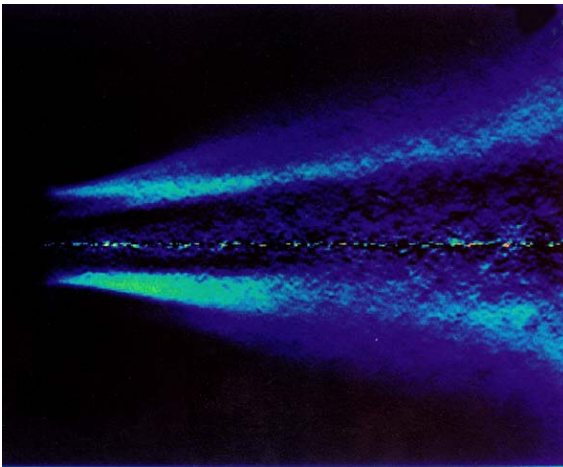


Figure 33. Deconvolution of the flame-emission of the OH-radical.

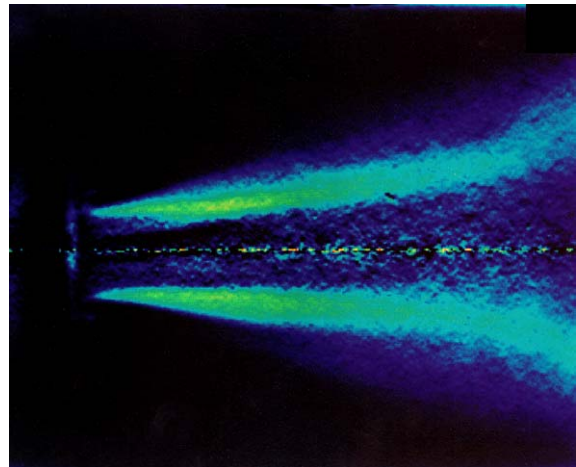


Figure 34. Deconvolution of the flame-emission of the H₂O-radical.

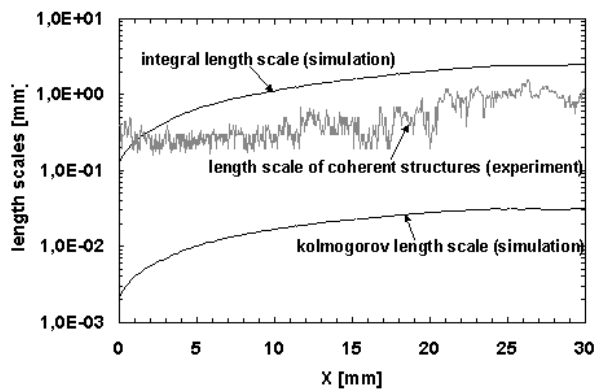


Figure 35. Comparison between numerical and simulated length scales and the correlated lengths scales

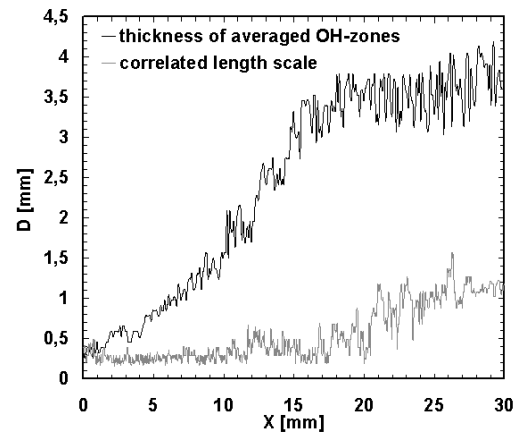


Figure 36. Thickness of averaged OH-zones and length scales for OH-correlations

3.2.2 CARS thermometry

The application of Coherent Anti-Stokes Raman Spectroscopy (CARS) to high pressure O_2/H_2 -combustion is not a straightforward task, see Eckberth [45]. The method has been developed at the DLR Lampoldshausen to a level that allows the application of CARS-thermometry to rocket model-combustors at the test facility P8 for the investigation of supercritical combustion (Clauß et al. [46], Smirnov et al. [47], Clauss et al. [48]) Only a short summary is given here as further detail concerning the application of CARS for thermometry to supercritical combustion can be found in Candel et al [49].

The temperature in the near injector region has been determined within the windowed combustion chamber "C" at a combustion chamber pressure of 6MPa and can be found in Smith et al. [50]. Measurements have been recorded at two radial profiles at two axial locations (see Figure 37). The results are summarized in Fig. 38. At $x = 50\text{mm}$ the average temperature is rather constant and near to 400K. Taking into regard the distribution of the OH-emission indicating chemical activity in this region, this low temperature level may be surprising. From shadowgraph images it is known that the O_2 -core is still compact in this region; only a minor fraction of O_2 is convected into the mixing region.

The combustor windows are protected by H_2 -film-cooling at ambient temperature and the mixture in the measurement volumes at $x = 50\text{mm}$ is therefore hydrogen-rich. The temperature is reduced due to the significant hydrogen excess to around 400K. At $x = 80\text{mm}$ a fluctuation of the temperature from laser shot to laser shot has been recorded, resulting in a bi-modal probability density function for the temperature. The low temperature peak was centered around 400K, and the high temperature component showed a variation with the radial location with a maximum average near to $r = 8\text{mm}$ of 1100K. Random single shot measurements at this location were in excess of 2000K. The strong bi-modal temperature distribution reflects the alternating convection of hot and cold gas volumes through the measurement volume. This finding is consistent with observation of an oscillating O_2 -core in the shadowgraphs.

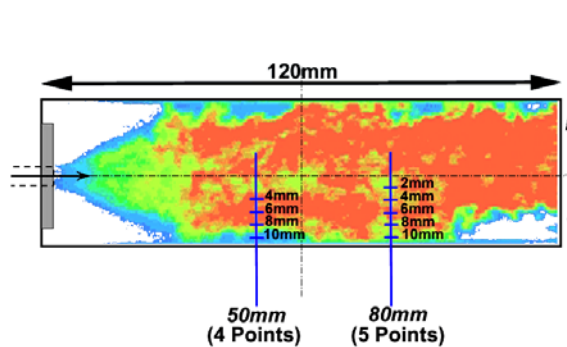


Figure 37: Measurement locations for CARS thermometry in windowed combustion chamber "C"

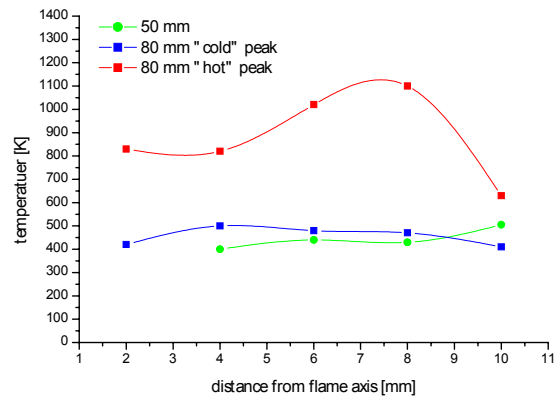


Figure 38: Radial profiles of the mean temperature values for axial positions 50mm and 80mm.

3.2.3 Dynamic pressure recordings

The pressure in a combustion chamber shows a variation around the mean value due to the turbulent characteristics of the mixing and combustion processes. In a test campaign dedicated to heat transfer measurements the dynamic pressure was analyzed for sub- and supercritical pressure conditions in a multi-injector combustor by Woschnak et al. [51]. The chamber was operated with cryogenic H_2/O_2 at a mixture ratio $R_{OF}=5$. Fourier transformed spectra of the combustion chamber noise are shown in Fig. 39.

The spectra, which were highly reproducible, show peaks corresponding to various chamber eigenmodes. Remarkable in this context is the significant difference in the intensity on the individual modes for sub- and supercritical pressure operating conditions. Although no thorough understanding exists to clearly explain this finding today, the result indicates that the interaction of acoustic waves with the atomization and mixing processes in the combustor is dependent on whether O_2 is injected at sub- or supercritical conditions. This finding is in agreement to the cold-flow acoustic interactions presented earlier in works by Chehrودي and Talley [34]. This response has also been observed with the windowed combustion chamber. This phenomenon requires further investigation under combusting conditions.

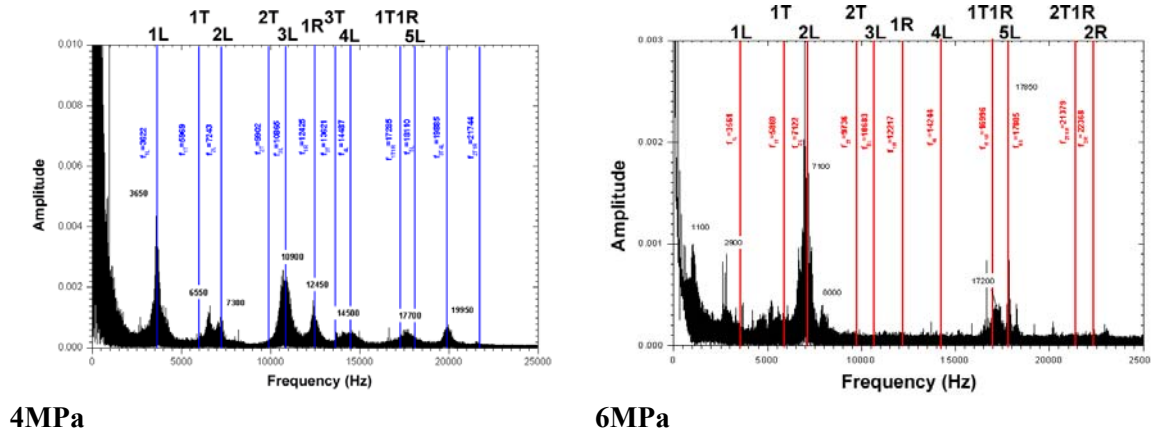


Figure 39: Fourier spectra of combustion chamber pressure at 4MPa and 6MPa in a multi-injector combustion chamber

4 Summary and Conclusions

Systematic research works designed to understand atomization, mixing, and combustion of a coaxial injector element in a cryogenic rocket at DLR and AFRL have so far revealed the following information;

Injection of liquid nitrogen under non-reacting conditions without co-flow gas into a chamber whose ambient pressure is varied to values exceeding the critical pressure was examined. Results from visualization, jet initial growth rate, fractal analysis, Raman scattering, and visible length scale measurements indicated that the injected fluid changes from liquid spray-like to gaseous jet-like behavior as pressure increases. This is attributed to the reduction of the surface tension and enthalpy of vaporization as the critical pressure of the injectant is approached.

The initial divergence angle indicating the growth rate of the jet was measured at the jet exit. These values were then compared with those measured from a large number of other mixing layer flows, including atomized liquid sprays, turbulent incompressible gaseous jets, supersonic jets, and incompressible but variable density jets covering over four orders of magnitude in the gas-to-

liquid density ratio. At and above the critical pressure of the injected fluid, the jet initial growth rate measurements agreed well with the theory and measurements of incompressible, variable density, gaseous mixing layers. The initial growth rate using Raman scattering was also in reasonably good agreement with measurements using shadowgraphy if twice the FWHM of the normalized intensity radial profiles are used. A visible length scale was calculated from images that showed good agreement with computed Taylor length scale using a $k-\epsilon$ model. An equation based on a proposed physical mechanism combined with the characteristic gasification time (τ_g) and interfacial bulge formation/separation time (τ_b) is proposed, $\theta = 0.27[(\tau_b / (\tau_b + \tau_g)) + (\rho_g / \rho_l)^{0.5}]$, that shows good agreement with the measured initial growth rate data.

It was found that the transition point from sub- (liquid-jet like) to supercritical (gas-jet like) behavior occurs when the time scale ratio ($\tau_b / (\tau_b + \tau_g)$) is approximately equal to 0.5. Interaction of the acoustic waves with the jet to gain insight on combustion instability revealed that the jet is strongly affected when injected into sub- and near- critical conditions with minimal interaction at supercritical ambient pressures. This finding corresponds to combustor response results at sub- and supercritical pressure with a multiple high pressure combustion chamber. Amplitudes from chamber pressure frequency spectra have consistently shown significant differences above and below the thermodynamic critical point of the injectants.

Advanced laser diagnostics were implemented under high pressure combustor conditions with LOX/H₂ to measure temperature at a range of points in the combustor. OH emission was measured in the high pressure combustion providing an indication of the combustion zones. The flame was typically anchored to the injector oxygen post. Length and time scales were derived under such conditions from experimental data. Quantitative diagnostics such as these provide further understanding regarding high pressure cryogenic combustion. Such data can be used to understand physical processes and to validate and assess numerical models developed by other groups.

5. References

- 1 Lefebvre, A., *Atomization and Sprays*, Hemisphere Publishing Corporation, New York, ISBN 0-89116-603-3, 1988, pp. 37-58.
- 2 Pitts, W., "Effects of global density and Reynolds number variations on mixing in turbulent, axisymmetric jets," NBSIR 86-3340, 1986.
- 3 Delplanque, J.-P. and Sirignano, W.A., "Numerical study of the transient vaporization of an oxygen droplet at sub- and supercritical conditions," *Int. J. Heat Mass Transfer*, Vol. 36, 1993, pp. 303-314.
- 4 Nicoli, C., Haldenwang, P., Daou, J., "Substitute mixtures for LOX droplet vaporization study," *Combustion Science and Technology*, Vol. 12, 1996, pp. 55-74.
- 5 Street, W.B., Calado, J.C.G., "Liquid-vapor equilibrium for hydrogen and nitrogen at temperatures from 63 to 100 K and pressures to 57 MPa," *J. Chem. Therm.*, Vol. 10, 1978, pp. 1089-1100.
- 6 Tully, DeVaney, Rhodes, "Phase equilibria of the Helium-Nitrogen system from 122 to 126 K," *Advanced Cryogenic Engineering*, U.S. Bureau of Mines, Vol. 16, 1970, pp. 88-95, Helium Research Center, Amarillo, Texas.
- 7 Macleod, D.B., "Relation between surface tension and density," *Transactions of the Faraday Society*, 19, 38, 1923.
- 8 Oswald, M. and Schik, A. "Supercritical Nitrogen Free Jet Investigated by Spontaneous Raman Scattering," *Experiments in Fluids*, 27, 1999, pp. 497-506.
- 9 Branam, R. and Mayer, W. "Characterization of Cryogenic Injection at Supercritical Pressure," *J. Of Propulsion and Power*, AIAA, Vol. 19, No. 3, May-June 2003.
- 10 Chehroudi, B, R. Cohn, R. , Talley, D. and Badakhshan, A. 2000. Raman Scattering Measurements in the Initial Region of Sub- and Supercritical Jets, AIAA Paper 2000-3392.
- 11 Chehroudi, D. Talley, and E. Coy, 'Initial growth rate and visual characteristics of a round jet into a sub- to supercritical environment of relevance to rocket, gas turbine, and diesel engines, *37th AIAA Aerospace Science Meeting and Exhibit*, AIAA 99-0206, Reno, NV, 11-14 January.
- 12 Chehroudi, B., Talley, D.G., and Coy, E.B., 2002. "Visual Characteristics and Initial Growth Rates of Round Cryogenic Jets at Supercritical and Supercritical Pressures," *Physics of Fluids*, Vol. 14, No. 2.
- 13 Chen, C. J. and Rodi, W. "Vertical Turbulent Buoyant Jets- A Review of Experimental Data. 1980, Pergamon.
- 14 Papanicolaou, P. N. and List, E. J. "Investigations of round vertical turbulent buoyant jets," *J. Fluid Mech.*, 195, 1988, pp. 341-391.
- 15 Reitz, R.D. and Bracco, F.V. On the dependence of spray angle and other spray parameters on nozzle design and operating condition, SAE Paper no. 790494, 1979.
- 16 Mayer, W., Schik, A., Schweitzer, C., and Schaffler, M., Injection and mixing processes in high pressure LOX/GH2 rocket combustors, AIAA Paper No. 96-2620, *32nd AIAA/ASME/SAE/ASEE Joint Propulsion Conference & Exhibit*, Lake Buena Vista, Florida, 1996.

- 17 Mayer, W., Ivancic, A., Schik, A., and Hornung, U., Propellant atomization in LOX/GH₂ rocket combustors, AIAA Paper No. 98-3685, *34th AIAA/ ASME/SAE/ASEE Joint Propulsion Conference & Exhibit*, Cleveland, Ohio, 13-15 July, 1998.
- 18 Abramovich, G. N., *The Theory of Turbulent Jets*, MIT Press, Cambridge, 1963.
- 19 Chehroudi, B., Chen, S. H. Bracco, F. V., and Y. Onuma, "On the intact core of full-cone sprays, Society of Automotive Engineers," 1985 Congress and Exposition, SAE Transaction Paper 850126, 25 February–1 March 1995.
- 20 Chehroudi, B., Talley, D.G., and Coy, E. B., Fractal geometry and growth rate of cryogenic jets near critical point, AIAA Paper 99-2489, 1999.
- 21 Brown, G. and Roshko, A. "On density effects and large structure in turbulent mixing layers, J. Fluid Mech., vol. 64, part 4, 1974, pp. 775-816.
- 22 Brown, G., 'The entrainment and large structure in turbulent mixing layers,' *5th Australian Conference on Hydraulics and Fluid Mechanics*, 1974, pp. 352–359.
- 23 Papamoschou, D. and Roshko, A. "The compressible turbulent shear layer: an experimental study," *J. Fluid Mech.*, vol. 197, 1988, pp. 453-477
- 24 Dimotakis, P.E. 'Two-dimensional shear-layer entrainment,' *AIAA Journal*, 21, No. 11, 1986, pp. 1791-1796
- 25 Oschwald, M. and Micci, M. Spreading angle and centerline variation of density of supercritical nitrogen jets, *Atomizations and Sprays*, vol. 11. pp. 91-106, 2002.
- 26 Mandelbrot, B. B., The Fractal Geometry of Nature, W. H. Freeman and Company, San Francisco, 1983.
- 27 Sreenivasan, K. R. and Meneveau, C. "The fractal facets of turbulence," *J. Fluid Mech.*, Vol. 173, 1986, pp. 357-386.
- 28 Dimotakis, P. E., Miake-Lye, W. G., and Papantoniou, D. A., *Phy. Fluids*, 26, p. 3185.
- 29 Taylor, J. J. and Hoyte J.W. 'Water jet photography-technique and methods,' *Exp. Fluids*, vol. 1, pp. 113-120, 1983.
- 30 Decker, M C, Schik, A, Meier, U E, Stricker R W. "Quantitative Raman Imaging Investigations of Mixing Phenomena in High Pressure Cryogenic Jets," *Appl Opt* 37:5620-5627, 1998.
- 31 Wygnanski, I and Fiedler, H. E. "The two-dimensional Mixing region," *J. Fluid Mech.*, 41, 327, 1970.
- 32 So, R M C, Zhu, J Y, Otugen, M V, and Hwang, B C, "Some Measurements in a Binary Gas Jet," *Experiments in Fluids*, 9, 273-284, 1990.
- 33 Oefelein J. C. and Yang, V. Comprehensive review of liquid propellant combustion instabilities in F-1 engines, *Journal of Propulsion and Power*, Vol. 9, No. 5, 1993, pp.657-677.
- 34 Chehroudi, B. and Talley, D., Interaction of acoustic waves with a cryogenic nitrogen jet at sub- and supercritical pressures, 40th AIAA Aerospace Sciences Meeting & Exhibit, AIAA 2002-0342, Reno, Nevada, 14-17 January 2002.

- 35 Tseng, L.-K., Ruff, G. A., P.-K., Wu, Faeth, G. M. 'Continuous- and dispersed-phase structure of pressure-atomized sprays," *Progress in Astronautics and Aeronautics: Recent Advances in Spray Combustion*, February, 1995.
- 36 Telaar, J., Schneider, G., Mayer, W., "Experimental investigation of breakup of turbulent liquid jets", ILASS-Europe 2000, Darmstadt, September 11-13, 2000
- 37 Oswald, M., Schik, A., Klar, M., Mayer, W., "Investigation of coaxial LN2/GH2-injection at supercritical pressure by spontaneous Raman scattering", AIAA 99-2887, 35th Joint Propulsion Conference and Exhibit, Los Angeles, Ca, 1999
- 38 Chehroudi, B., Davis, D., and Talley, D., Initial Results From A Cryogenic Coaxial Injector In An Acoustic Field," 41st AIAA Aerospace Sciences Meeting & Exhibit, Reno, Nevada, Paper AIAA-2003-1339, 6-9 January, 2003.
- 39 Yang, V., "Droplet behavior at supercritical conditions," *Recent Advances in Spray Combustion: Spray Atomization and Drop Burning*, Vol. 1, AIAA Progress in Aeronautics and Astronautics, Vol. 166, 1995, pp. 413-437
- 40 Mayer, W., and Smith, J., "Fundamentals of supercritical mixing and combustion of cryogenic propellants," Rocket Engine Thrust Chambers, AIAA Progress in Aeronautics and Astronautics (in press)
- 41 Mayer, W., Tamura, H., "Propellant injection in a liquid oxygen/gaseous hydrogen rocket engine," *Journal of Propulsion and Power*, Vol. 12, No. 6, 1996, pp. 1137-1147
- 42 Mayer, W., Schik, A., Vielle, B., Chaveau, C., Gökalp. I., Talley, D. "Atomization and Breakup of cryogenic propellants under high pressure subcritical and supercritical conditions," *Journal of Propulsion and Power*, Vol. 14, No. 5, 1998, pp. 835-842
- 43 Mayer, W., Tamura, H., "Flow Visualization of supercritical propellant injection in a firing LOX/GH2 rocket engine", AIAA 95-2433, 31st Joint Propulsion Conference and Exhibit, San Diego, Ca, 1995
- 44 Ivancic, B., Mayer, W., "Time and lengths scales of mixing and and combustion processes in high pressure LOX/GH2-rocket combustors," *Journal of Propulsion and Power*, Vol. 18, No.2, 2002, pp. 247-253.
- 45 Eckbreth, A., Laser diagnostics for combustion, Temperature and Species, Gordon and Breach, Amsterdam, 1996
- 46 Clauß, W., Kozlov, D. N., Pykhov, R. L., Smirnov, V. V., Stel'makh, O. M., Vereshagin, K. A., "The Analysis of the Precision of Single Shot 2λ -CARS Temperature Measurements in Hydrogen," *Appl. Phys. B* 65, 619-624, 1997
- 47 Smirnov, V.V., Clauss, W., Oswald, M., Grisch, F., Bouchardy, P., "Theoretical and Practical Issues of CARS Application to Cryogenic Spray Combustion," 4th International Symposium of Liquid Space Propulsion, Heilbronn, March 13-15, 2000
- 48 Clauss, W., Vereschagin, K.A., Klimenko, D.N., Oswald, M., Smirnov, V.V., Stelmakh, O.M., Fabelinski, V.I., "CARS Investigation of Hydrogen Q-Branch Linewidths at High Temperatures in a High-Pressure H2/O2-Burner," *Journal of Raman Spectroscopy*, 33, 2002, pp. 906-911
- 49 Candel S. et al., Grisch F. et al., Oswald M. et al., "Investigation of transcritical cryogenic combustion using imaging and laser techniques," 5th International Symposium on Liquid Space Propulsion, Chattanooga, TN, October 27-30, 2003

- 50 Smith, J., Klimenko, D., Clauss, W., and Mayer, W., "Supercritical LOX/Hydrogen Rocket Combustion Investigations using Optical Diagnostics," AIAA 2002-4033
- 51 Woschnak, A., Suslov, D., Oswald, M., "Experimental and numerical investigation of thermal stratification effects," AIAA 2003-3214, Joint Propulsion Conference, Huntsville, 2003

6. Acknowledgements

The DLR and AFRL would like to acknowledge all those who have been involved in the research programs. These people include colleagues at the test bench and technicians who have helped make these studies possible.